ARTICLE

Endothelial LRP1 protects against neurodegeneration by blocking cyclophilin A

Angeliki Maria Nikolakopoulou[1]*, Yaoming Wang[1]*, Qingyi Ma[1]*, Abhay P. Sagare[1], Axel Montagne[1], Mikko T. Huuskonen[1], Sanket V. Rege[1], Kassandra Kisler[1], Zhonghua Dai[1], Jakob Körbelin[2], Joachim Herz[3,4], Zhen Zhao[1]**, and Berislav V. Zlokovic[1]**

The low-density lipoprotein receptor–related protein 1 (LRP1) is an endocytic and cell signaling transmembrane protein. Endothelial LRP1 clears proteinaceous toxins at the blood–brain barrier (BBB), regulates angiogenesis, and is increasingly reduced in Alzheimer's disease associated with BBB breakdown and neurodegeneration. Whether loss of endothelial LRP1 plays a direct causative role in BBB breakdown and neurodegenerative changes remains elusive. Here, we show that LRP1 inactivation from the mouse endothelium results in progressive BBB breakdown, followed by neuron loss and cognitive deficits, which is reversible by endothelial-specific *LRP1* gene therapy. LRP1 endothelial knockout led to a self-autonomous activation of the cyclophilin A–matrix metalloproteinase-9 pathway in the endothelium, causing loss of tight junctions underlying structural BBB impairment. Cyclophilin A inhibition in mice with endothelial-specific LRP1 knockout restored BBB integrity and reversed and prevented neuronal loss and behavioral deficits. Thus, endothelial LRP1 protects against neurodegeneration by inhibiting cyclophilin A, which has implications for the pathophysiology and treatment of neurodegeneration linked to vascular dysfunction.

Introduction

Low-density lipoprotein receptor–related protein 1 (LRP1) is a transmembrane endocytic and cell signaling protein that regulates diverse cellular functions in the brain, liver, kidney, lung, and vasculature (Lillis et al., 2008; Gonias and Campana, 2014). LRP1 was cloned and identified as an apolipoprotein E (apoE) receptor (Herz et al., 1988) with a role in lipoprotein metabolism (Lillis et al., 2008). Besides functioning as an endocytic receptor for 100 diverse ligands, LRP1 binds different cell signaling adapter and scaffold proteins via its cytoplasmic tail, interacts with different receptors and plasma membrane proteins, and activates signaling responses upon binding different ligands (Lillis et al., 2008; Herz and Strickland, 2001; Bell et al., 2012; Mantuano et al., 2013).

In the cerebral vascular system, endothelial LRP1 regulates transendothelial clearance of several neurotoxins across the blood–brain barrier (BBB), including Alzheimer's amyloid-β (Shibata et al., 2000; Deane et al., 2004; Yamada et al., 2008; Zhao et al., 2015b; Winkler et al., 2015; Storck et al., 2016; Zhu et al., 2018; Shin et al., 2019). It also controls angiogenesis in the retina (Mao et al., 2016; Strickland and Muratoglu, 2016). Additionally, endothelial LRP1 directly participates in gene transcription in endothelial cells acting as a transcriptional coactivator of the nuclear receptor PPARγ, a central regulator of lipid and glucose metabolism, suggesting its role in maintaining energy homeostasis (Mao et al., 2017).

Endothelial LRP1 is reduced by aging and is almost absent from blood vessels in Alzheimer's disease (AD) in humans (Shibata et al., 2000; Deane et al., 2004; Donahue et al., 2006; Halliday et al., 2016) and animal models (Deane et al., 2004; Zhao et al., 2015b; Winkler et al., 2015; Jaeger et al., 2009). Its loss is associated with BBB breakdown, which has been shown to be an early biomarker of human cognitive dysfunction (Montagne et al., 2015; Nation et al., 2019; Montagne et al., 2020) and AD (Sweeney et al., 2018), and is also related to neuronal dysfunction in animal models of AD (Zhao et al., 2015b; Winkler et al., 2015). Whether loss of endothelial LRP1 plays a direct causative role in BBB breakdown and neurodegenerative changes remains, however, elusive. To address this question, we

---

[1]Department of Physiology and Neuroscience, Zilkha Neurogenetic Institute, Keck School of Medicine, University of Southern California, Los Angeles, Los Angeles, CA; [2]Hubertus Wald Cancer Center, Department of Oncology and Hematology, University Medical Center Hamburg-Eppendorf, Hamburg, Germany; [3]Departments of Neuroscience, Molecular Genetics, and Neurology, University of Texas Southwestern Medical Center, Dallas, TX; [4]Center for Neuroscience, University of Freiburg, Freiburg, Germany.

*A.M. Nikolakopoulou, Y. Wang, and Q. Ma contributed equally to this paper; **Z. Zhao and B.V. Zlokovic contributed equally to this paper; Correspondence to Berislav V. Zlokovic: zlokovic@usc.edu.

https://doi.org/10.1084/jem.20202207

studied BBB integrity, neuronal phenotype, and behavior in an endothelial-specific *Lrp1* knockout line generated by crossing *Lrp1*$^{lox/lox}$ mice (Boucher et al., 2003) with an endothelial-specific *Tie2-Cre* line (Kisanuki et al., 2001).

Results

BBB breakdown and neuronal phenotype

Consistent with multiple previous independent reports demonstrating expression of LRP1 protein in brain endothelial cells by immunostaining, Western blotting, and/or immunogold electron microscopy in different species, including mice, rats, humans, bovines, and porcine (Shibata et al., 2000; Deane et al., 2004; Yamada et al., 2008; Zhao et al., 2015b; Winkler et al., 2015; Storck et al., 2016; Zhu et al., 2018; Shin et al., 2019; Mao et al., 2016; Strickland and Muratoglu, 2016; Donahue et al., 2006; Halliday et al., 2016; Jaeger et al., 2009; Wang et al., 2003; Demeule et al., 2008; Ueno et al., 2010; Pflanzner et al., 2011; Gali et al., 2019; Wu et al., 2020), we also show by immunoblotting with an LRP1-specific antibody (Fig. 1 A) and quantitative real-time PCR for *Lrp1* mRNA relative to *Gapdh* (housekeeping gene; Fig. 1, B and C) that brain endothelial cells from *Lrp1*$^{lox/lox}$ littermate control mice express both LRP1 protein and *Lrp1* mRNA. Of note, brain endothelial cell cultures had typical cobblestone-like shape and were positive for endothelial cell markers (including von Willebrand factor, CD31, and vascular endothelial-cadherin) and negative for pericyte markers (PDGFRβ, CD13, and NG2), vascular smooth muscle cell markers (α-smooth muscle actin), astrocyte markers (GFAP and AQP4), neuronal markers (MAP2 and NeuN), and the microglia marker Iba1, as we previously reported (Bell et al., 2012; Zhao et al., 2015b). Compared with *Lrp1*$^{lox/lox}$ controls, brain endothelial cells from *Lrp1*$^{lox/lox}$*; Tie2-Cre* mice had complete deletion of LRP1 protein and *Lrp1* mRNA, as shown by immunoblotting (Fig. 1 A) and quantitative real-time PCR (Fig. 1, B and C), respectively. Additionally, we found gene dose–dependent loss of LRP1 and *Lrp1* mRNA from brain endothelium in *Lrp1*$^{lox/+}$*; Tie2-Cre* (lox/+) and *Lrp1*$^{lox/lox}$*; Tie2-Cre* (lox/lox) mice, respectively. In contrast, brain capillary pericytes from *Lrp1*$^{lox/+}$*; Tie2-Cre* (lox/+) and *Lrp1*$^{lox/lox}$*; Tie2-Cre* (lox/lox) mice expressed LRP1 protein and *Lrp1* mRNA at levels comparable to their *Lrp1*$^{lox/lox}$ littermate controls (Fig. 1, D–F).

Expression of LRP1 in endothelium of brain capillaries isolated from control *Lrp1*$^{lox/lox}$ mice, and its loss from endothelium in *Lrp1*$^{lox/lox}$*; Tie2-Cre* mice, was confirmed by triple immunofluorescent staining for LRP1, the brain endothelial-specific marker CD31, and the pericyte-specific marker CD13 (Fig. 1 G), including the orthogonal views of different planes (xz, yz) of higher magnification confocal images of LRP1 and CD31 (Fig. 1 H). Brain endothelial expression of LRP1 in *Lrp1*$^{lox/lox}$ mice and its loss from endothelium in *Lrp1*$^{lox/lox}$*; Tie2-Cre* mice were independently confirmed using GLUT1 as another endothelial-specific marker (Fig. 1 I).

First, we found that 2-mo-old *Lrp1*$^{lox/lox}$*; Tie2-Cre* mice develop a spontaneous BBB breakdown, as illustrated by the presence of the perivascular capillary deposits of blood-derived IgG and fibrinogen in the cortex (Fig. 2 A). Quantification analysis indicated that 2-mo-old *Lrp1*$^{lox/lox}$*; Tie2-Cre* mice had in average 8–10 and 8–6 times greater accumulation of IgG and fibrinogen deposits in the cortex and hippocampus, respectively, than their *Lrp1*$^{lox/lox}$ littermate controls (Fig. 2, B and C). When compared with 2-mo-old mice, 4-mo-old *Lrp1*$^{lox/lox}$*; Tie2-Cre* mice exhibited a further increase in IgG and fibrinogen deposits (Fig. 2, B and C). Progressive BBB breakdown in 2- and 4-mo-old *Lrp1*$^{lox/lox}$*; Tie2-Cre* mice compared with *Lrp1*$^{lox/lox}$ littermate controls has been confirmed in vivo by two-photon imaging of intravenously administered 40-kD FITC-dextran leakage from the cortical capillaries (Fig. 2, D and E) and by tissue accumulation of intravenously administered Alexa Fluor 555–cadaverine (mol wt = 950 daltons), suggesting a substantial cortical uptake of this tracer in mice with endothelial-specific LRP1 knockout (Fig. 2, F and G).

At postnatal day P8, *Lrp1*$^{lox/lox}$*; Tie2-Cre* mice had, however, intact BBB to Alexa Fluor 555–cadaverine, showing no leakage of this tracer into the cortex (Fig. S1 A, upper panel) or retina (Fig. S1 A, lower panel), thus ruling out BBB breakdown during development as a possible cause of BBB breakdown in adult *Lrp1*$^{lox/lox}$*; Tie2-Cre* mice. Additionally, *Lrp1*$^{lox/lox}$*; Tie2-Cre* and control mice had comparable cortical capillary length and number of branching points (Fig. S1, B and C). Consistent with these data, 2-mo-old *Lrp1*$^{lox/lox}$*; Tie2-Cre* and control mice had also comparable cortical capillary length (Fig. S1 D), suggesting that there is no reduction in vascular density in these mice. In contrast, we found that BBB breakdown in *Lrp1*$^{lox/lox}$*; Tie2-Cre* mice develops at earlier time points between P8 and 2 mo of age (Fig. 2, A–G) and becomes detectable in 1-mo-old *Lrp1*$^{lox/lox}$*; Tie2-Cre* mice, as we shown by both fibrinogen deposits and accumulation of intravenously administered Alexa Fluor 555–cadaverine (Fig. S1, E and F).

Lrp1$^{lox/lox}$*; Tie2-Cre* and control mice had similar cortical and hippocampal capillary coverages of lectin$^+$ endothelial profiles by pericytes and/or astrocytic endfeet (Fig. S2, A–F). They also expressed comparable levels of endothelial transporters known to influence BBB integrity such as major facilitator superfamily domain–containing protein 2 (Fig. S2, G and H; Ben-Zvi et al., 2014) and glucose transporter 1 (Fig. S2, I and J; Winkler et al., 2015). Thus, BBB breakdown as seen in *Lrp1*$^{lox/lox}$*; Tie2-Cre* mice could not be attributed to changes in pericyte and/or astrocyte coverage or expression of other BBB-regulating transporters.

Next, we found that 2-mo-old *Lrp1*$^{lox/lox}$*; Tie2-Cre* mice had normal number of neurons and neuritic density, but at 4 mo of age, they developed a substantial loss of NeuN$^+$ neurons compared with controls (~30%) and loss of SMI312$^+$ neurites (~35%) both in the cortex and hippocampus (Fig. 2, H–J), suggesting that neuronal degeneration develops after BBB breakdown. Consistent with these data, daily activity behavior tests burrowing and nest building, and hippocampal memory tests novel object location and recognition were normal in 2-mo-old *Lrp1*$^{lox/lox}$*; Tie2-Cre* mice, but all showed deficits in 4-mo-old *Lrp1*$^{lox/lox}$*; Tie2-Cre* mice compared with littermate controls (Fig. 2, K–N).

Brain endothelial LRP1 gene delivery

To test whether vascular and neuronal changes are reversible, we performed a rescue experiment using brain endothelial–specific

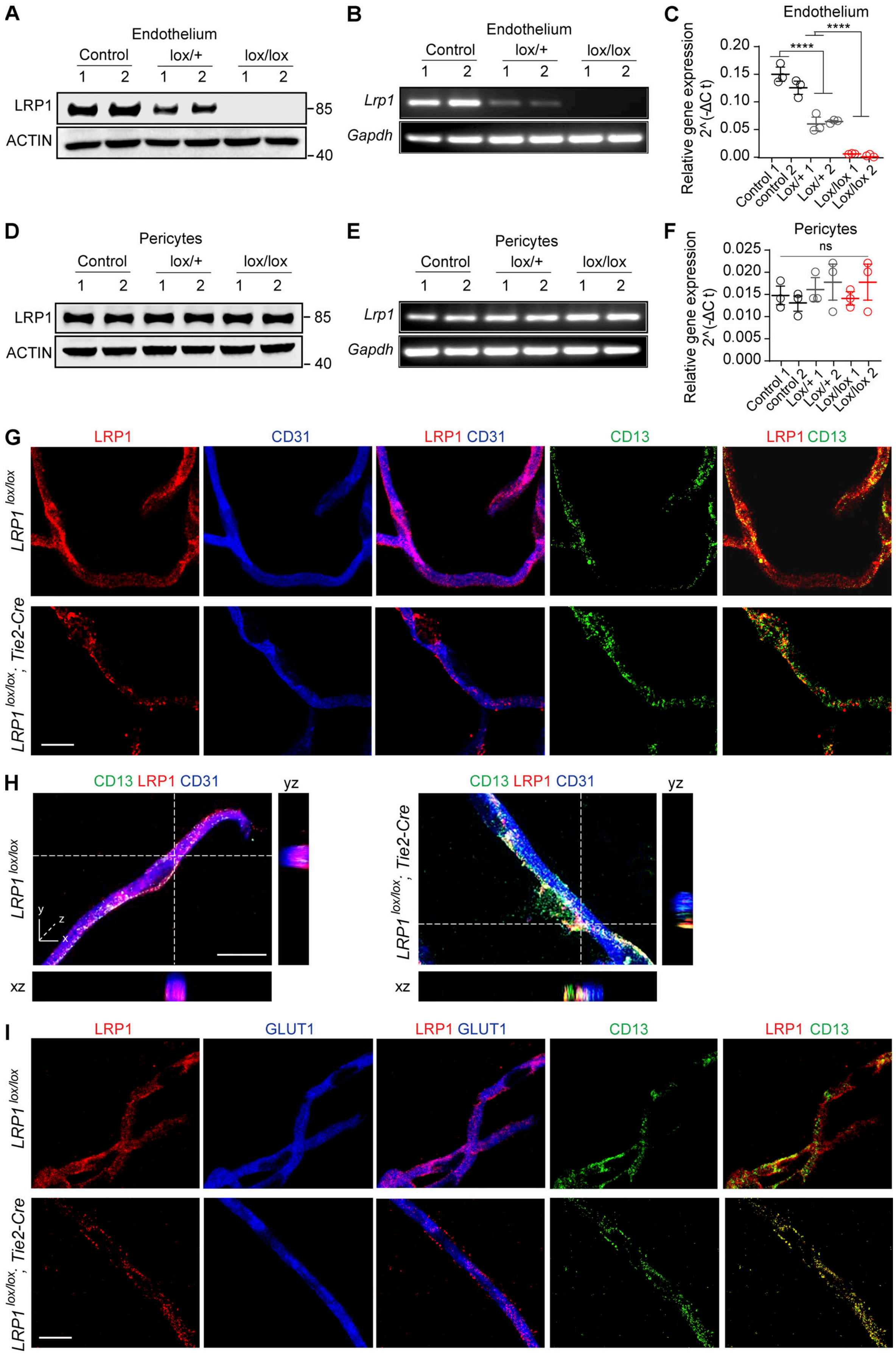
A
Endothelium
Control lox/+ lox/lox
1 2 1 2 1 2
LRP1
ACTIN
85
40
B
Endothelium
Control lox/+ lox/lox
1 2 1 2 1 2
Lrp1
Gapdh
C
Endothelium
Relative gene expression 2^(-ΔC t)
0.20 0.15 0.10 0.05 0.00
****
****
Control 1 control 2 Lox/+ 1 Lox/+ 2 Lox/lox 1 Lox/lox 2
D
Pericytes
Control lox/+ lox/lox
1 2 1 2 1 2
LRP1
ACTIN
85
40
E
Pericytes
Control lox/+ lox/lox
1 2 1 2 1 2
Lrp1
Gapdh
F
Pericytes
ns
Relative gene expression 2^(-ΔC t)
0.025 0.020 0.015 0.010 0.005 0.000
Control 1 control 2 Lox/+ 1 Lox/+ 2 Lox/lox 1 Lox/lox 2
G
LRP1 CD31 LRP1 CD31 CD13 LRP1 CD13
LRP1 lox/lox
LRP1 lox/lox; Tie2-Cre
H
CD13 LRP1 CD31 yz
LRP1 lox/lox
y z x
xz
CD13 LRP1 CD31 yz
LRP1 lox/lox; Tie2-Cre
xz
I
LRP1 GLUT1 LRP1 GLUT1 CD13 LRP1 CD13
LRP1 lox/lox
LRP1 lox/lox; Tie2-Cre

Figure 1. **Endothelial LRP1 expression and deletion in mice. (A–C)** LRP1 immunoblotting (#92544 mAb; Abcam; A), *Lrp1* mRNA quantitative real-time PCR (B), and relative *Lrp1* mRNA gene expression normalized to *Gapdh* (housekeeping gene; C) in brain endothelial cells cultured from *Lrp1*$^{lox/lox}$ littermate control mice (control), *Lrp1*$^{lox/+}$*; Tie2-Cre* (lox/+) and *Lrp1*$^{lox/lox}$*; Tie2-Cre* (lox/lox) mice. In C, for relative gene expression calculations, we used the 2^(−ΔCt) method, where Ct (cycle threshold) is defined as the number of cycles required for the fluorescent signal to cross the threshold (i.e., exceeds background level). With respect to the ΔCt of the 2^(−ΔCt) method, ΔCt is the difference in the threshold cycles between *Lrp1* and *Gapdh* genes. **(D–F)** LRP1 immunoblotting (D), *Lrp1* mRNA quantitative real-time PCR (E), and relative *Lrp1* mRNA gene expression normalized to *Gapdh* (F) in pericytes cultured from *Lrp1*$^{lox/lox}$ littermate control mice (control), *Lrp1*$^{lox/+}$*; Tie2-Cre* (lox/+), and *Lrp1*$^{lox/lox}$*; Tie2-Cre* (lox/lox) mice. Calculations in F were the same as in C. **(G)** Representative confocal images of triple immunofluorescent staining for LRP1, CD31 (endothelium), and CD13 (pericytes) showing expression of LRP1 in endothelium in isolated cortical capillaries from *Lrp1*$^{lox/lox}$ control mice and its deletion from endothelium in capillaries from *Lrp1*$^{lox/lox}$*; Tie2-Cre* (lox/lox) mice; purple, merged LRP1 and CD31 (endothelium); yellow, merged LRP1 and CD13 (pericytes). No changes in expression of LRP1 in pericytes were observed between control and *Lrp1*$^{lox/lox}$*; Tie2-Cre* (lox/lox) mice. Scale bar = 10 µm. **(H)** High-magnification orthogonal views showing colocalization of LRP1 with endothelial marker CD31 in brain capillaries from *Lrp1*$^{lox/lox}$ control mice (left) and loss of LRP1 from endothelium in brain capillaries from *Lrp1*$^{lox/lox}$*; Tie2-Cre* mice (right). CD13, pericyte marker. Scale bar = 15 µm. **(I)** Representative confocal images of triple immunofluorescent staining for LRP1, GLUT1 (endothelium), and CD13 (pericytes) showing expression of LRP1 in endothelium in isolated cortical capillaries from *Lrp1*$^{lox/lox}$ control mice and its deletion from endothelium in capillaries from *Lrp1*$^{lox/lox}$*; Tie2-Cre* (lox/lox) mice; purple, merged LRP1 and GLUT1 (endothelium); yellow, merged LRP1 and CD13 (pericytes). No changes in expression of LRP1 in pericytes were observed between control and *Lrp1*$^{lox/lox}$*; Tie2-Cre* (lox/lox) mice. Scale bar = 10 µm. In C and F, significance was determined by one-way ANOVA followed by Bonferroni post hoc test; ns, not significant; ****, $P < 0.0001$.

---

adeno-associated viral construct (AAV2-BR1; Körbelin et al., 2016) containing *LRP1* minigene (m*LRP1*) with LRPIV (low-density lipoprotein receptor–related protein cluster IV) extracellular domain and the cytoplasmic cell signaling tail, as reported previously (Zhao et al., 2015b). We chose to treat 3-mo-old *Lrp1*$^{lox/lox}$*; Tie2-Cre* mice, because these mice have a pronounced BBB breakdown (Fig. 2, B, C, E, and G) and begin developing a significant loss of neurons (16–19%) and neuritic density (15–19%), respectively (Fig. S3). AAV2-BR1-m*LRP1* virus efficiently transduced brain endothelial cells of *Lrp1*$^{lox/lox}$*; Tie2-Cre* mice, as shown by >45% colocalization of hemagglutinin (HA)–tagged mLRP1 with lectin^{+} endothelial capillary profiles in the cortex and hippocampus (Fig. 3, A and B). The transduction efficiency of mLRP1 was comparable to previously shown brain endothelial transduction efficiency of AAV2-BR1-*GFP* control vector (Körbelin et al., 2016). When compared with GFP control, mLRP1 endothelial reexpression in *Lrp1*$^{lox/lox}$*; Tie2-Cre* mice led to substantial reductions of IgG and fibrinogen accumulates in the cortex and hippocampus (Fig. 3, C–E). Quantification analysis revealed that *Lrp1*$^{lox/lox}$*; Tie2-Cre* mice treated with AAV2-BR1-m*LRP1* had in average ∼55% and 54% reductions in IgG deposits (Fig. 3 D) and 58% and 55% reductions in fibrinogen deposits (Fig. 3 E) in the cortex and hippocampus, respectively, compared with the respective leakages of IgG and fibrinogen in *Lrp1*$^{lox/lox}$*; Tie2-Cre* mice treated with the control AAV2-BR1-*GFP* construct. Reductions in leakages of blood-derived proteins in *Lrp1*$^{lox/lox}$*; Tie2-Cre* mice treated with AAV2-BR1-m*LRP1* corresponded well with the observed 45% transduction efficiency of mLRP1 (Fig. 3 B). A higher magnification analysis indicated that vessel segments that reexpressed HA-mLRP1 did not leak fibrinogen, whereas those that did not reexpress HA-mLRP1 leaked fibrinogen (Fig. 3 F).

Importantly, AAV2-BR1-*mLRP1* treatment compared with AAV2-BR1-*GFP* control increased the number of NeuN^{+} neuron and SMI312^{+} neuritic density in the cortex and hippocampus of *Lrp1*$^{lox/lox}$*; Tie2-Cre* mice nearly to the levels seen in *Lrp1*$^{lox/lox}$ littermate controls treated with AAV2-BR1-*mLRP1* or control AAV2-BR1-*GFP* virus (Fig. 3, G–I). When compared with AAV2-BR1-*GFP* control treatment, gene therapy with m*LRP1* also normalized behavior in *Lrp1*$^{lox/lox}$*; Tie2-Cre* mice on all four tests almost to the levels found in *Lrp1*$^{lox/lox}$ littermate controls treated with AAV2-BR1-*mLRP1* or control AAV2-BR1-*GFP* virus (Fig. 3, J–M). Since 3-mo-old *Lrp1*$^{lox/lox}$*; Tie2-Cre* mice had a detectable neuron loss (Fig. S3), these data suggest that the present mLRP1 gene therapy (1) restores the BBB integrity and lowers leakages of blood-derived proteins to levels below those seen in 2-mo-old *Lrp1*$^{lox/lox}$*; Tie2-Cre* mice (Fig. 2, B and C) associated with normal neuronal phenotype and behavior (Fig. 2, H–N) and (2) protects mice from neuron loss and corrects behavioral deficits as shown at 1 mo after treatment.

Activation of the cyclophilin A (CypA)–matrix metalloproteinase-9 (MMP9) pathway

In search of a mechanism underlying BBB breakdown, we found that 2-mo-old *Lrp1*$^{lox/lox}$*; Tie2-Cre* mice compared with *Lrp1*$^{lox/lox}$ littermate controls develop a substantial loss (>50%) of the endothelial tight junction proteins zonula occludens 1 (ZO-1), occludin, and claudin 5, as shown by simultaneous immunostaining for these tight junction proteins and endothelial-specific *Lycopersicon esculentum* lectin fluorescence staining (Fig. 4, A–D). Loss of tight junction proteins was confirmed independently by immunoblotting of cortical microvessels isolated from these mice (Fig. 4, E and F). Additionally, we found that mice with endothelial knockout of LRP1 have greatly reduced levels of collagen IV basement membrane protein and develop blood-derived hemosiderin deposits indicative of microhemorrhages, as shown by Prussian blue staining for iron (Fig. S4, A–D). Since claudin 5 deficiency results in leakages of small, but not large, tracers, as previously shown (Nitta et al., 2003), it is likely that loss of several tight junction proteins as well as collagen IV contributed to the observed BBB breakdown in *Lrp1*$^{lox/lox}$*; Tie2-Cre* mice.

Loss of endothelial tight junctions and collagen IV in *Lrp1*$^{lox/lox}$*; Tie2-Cre* mice phenocopied the defects in mice lacking murine apoE, an LRP1 ligand, and/or expressing human apoE4 (*APOE4*), which poorly interacts with LRP1 (Bell et al., 2012). *Apoe* null mice and *APOE4* knockin mice have normal levels of LRP1 in endothelium, pericytes, and astrocytes but have an early loss of cerebrovascular integrity because of a loss of signal transduction (Bell et al., 2012; Fullerton et al., 2001) and/or weak

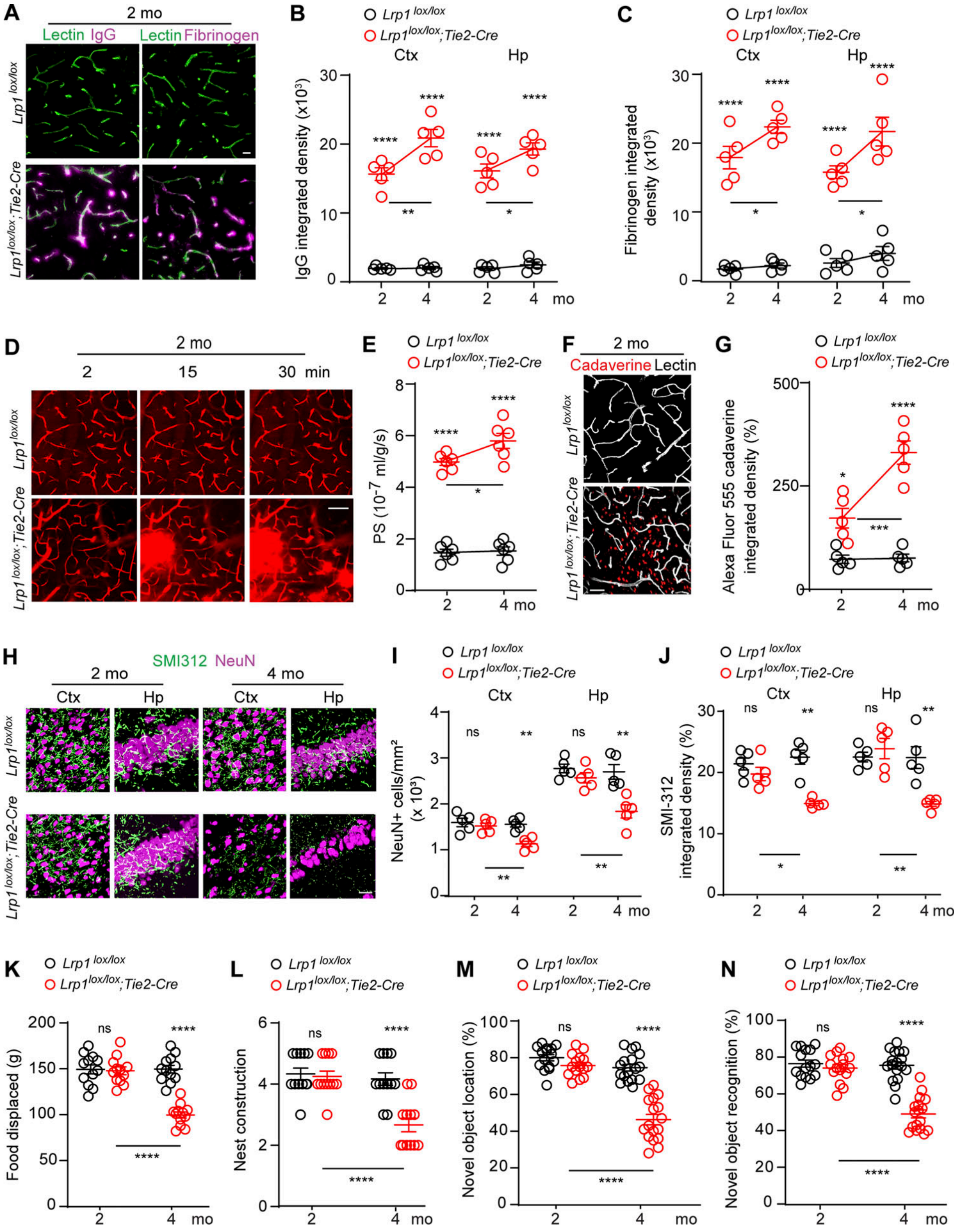

Figure 2. **BBB breakdown, neuron loss, and behavioral deficits after endothelial-specific *Lrp1* deletion. (A)** Immunostaining for IgG (left, purple), fibrinogen (right, purple), and lectin⁺ endothelium (green) shows perivascular capillary leakages of blood-derived proteins in the cortex of 2-mo-old *Lrp1*$^{lox/lox}$; *Tie2-Cre* mice compared with *Lrp1*$^{lox/lox}$ littermate controls. Scale bar = 20 µm. **(B and C)** Quantification of IgG (B) and fibrin (C) deposits in the cortex (Ctx) and hippocampus (Hp) in 2- and 4-mo-old *Lrp1*$^{lox/lox}$; *Tie2-Cre* mice and *Lrp1*$^{lox/lox}$ controls. Mean ± SEM, *n* = 5 mice/group. **(D and E)** Capillary leakages of intravenously administered 40 kD FITC-dextran in the cortex of 2-mo-old *Lrp1*$^{lox/lox}$; *Tie2-Cre* mice compared with *Lrp1*$^{lox/lox}$ control mice (D), and quantification of the BBB permeability–surface area product (PS) to 40 kD FITC-dextran in 2- and 4-mo-old mice (E). Scale bar = 50 µm. Mean ± SEM, *n* = 6 mice/group. **(F and G)** Cortical uptake of intravenously administered Alexa Fluor 555–cadaverine (red) in 2-mo-old *Lrp1*$^{lox/lox}$; *Tie2-Cre* and *Lrp1*$^{lox/lox}$ mice (F), and quantification of cadaverine cortical uptake in 2- and 4-mo-old mice (G). Scale bar = 25 µm. White, lectin⁺ endothelium. Mean ± SEM, *n* = 5 mice/group. **(H–J)** NeuN⁺ neurons and SMI312⁺ neurites (H), and quantification of NeuN⁺ neurons and SMI312⁺ neurites in the cortex and hippocampus in 2- and 4-mo-old *Lrp1*$^{lox/lox}$; *Tie2-Cre* and *Lrp1*$^{lox/lox}$ mice (I and J). Scale bar = 50 µm. Mean ± SEM, *n* = 5 mice/group. **(K–N)** Burrowing (K), nest construction (L), novel object location (M), and recognition (N) in 2- and 4-mo-old *Lrp1*$^{lox/lox}$; *Tie2-Cre* and *Lrp1*$^{lox/lox}$ mice. Mean ± SEM, *n* = 12 (K and L) and *n* = 15–17 (M and N) mice/group. In B, C, E, G, and I–N, significance was determined by one-way ANOVA followed by Bonferroni post hoc test; ns, not significant; *, $P < 0.05$; **, $P < 0.01$; ***, $P < 0.001$; ****, $P < 0.0001$. In B, C, E, and G, asterisks above red dots indicate comparisons with control group.

signal transduction (Bell et al., 2012) between astrocyte-derived apoE and human apoE4 with LRP1 on pericytes, respectively. This in turn has been shown to lead to transcriptional activation of the proinflammatory CypA–NF-κB–MMP9 pathway in pericytes, causing non–cell-autonomous MMP9-mediated degradation of tight junction proteins and collagen IV and leading to BBB breakdown (Bell et al., 2012). Thus, we next studied whether endothelial LRP1 deletion can lead to a cell-autonomous activation of the CypA–MMP9 pathway in the endothelium. We found elevated CypA and MMP9 levels in lectin⁺ endothelium in brain

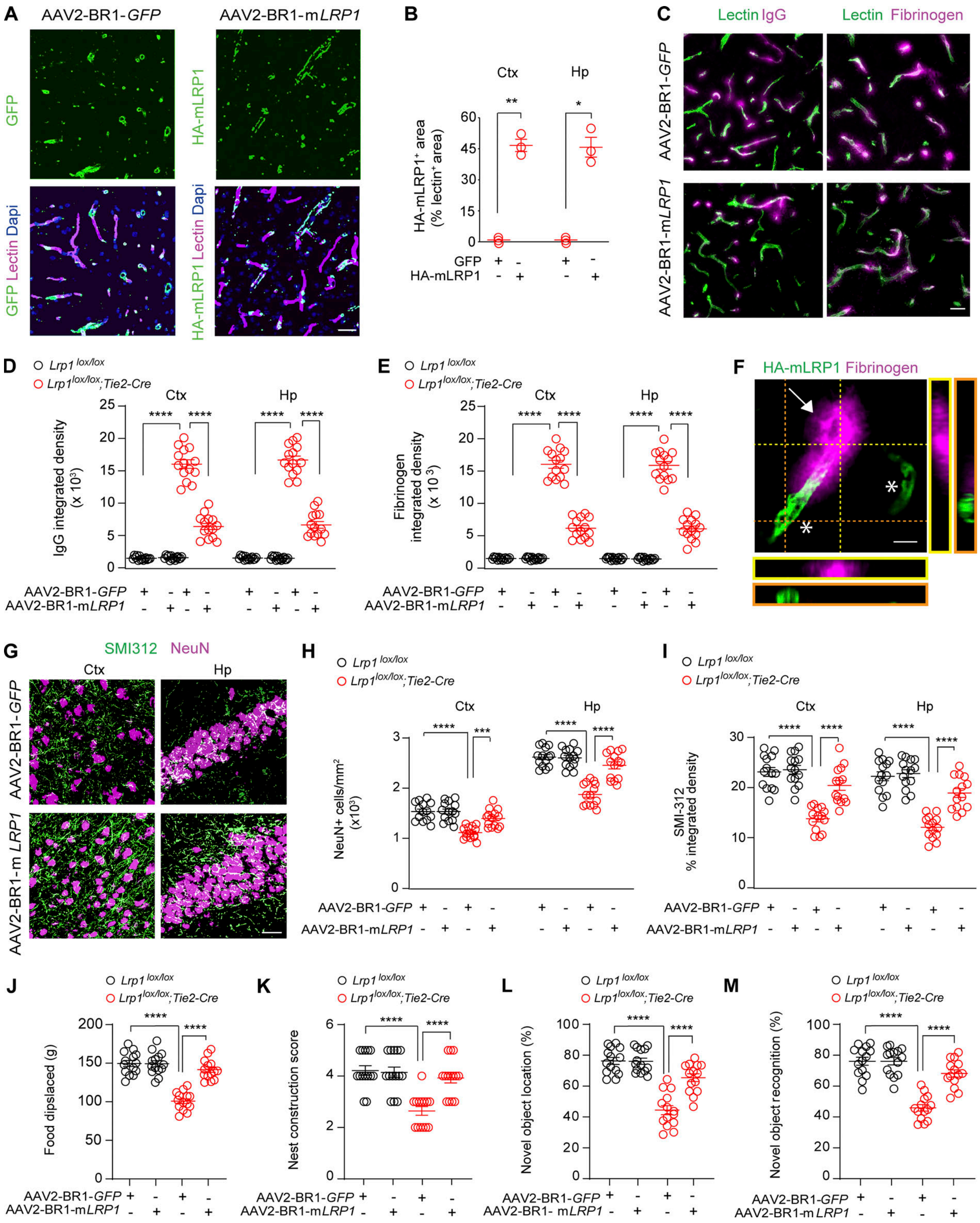

Figure 3. **Rescue of vascular and neuronal phenotype in *Lrp1*$^{lox/lox}$*; Tie2-Cre* mice by endothelial-specific *LRP1* gene replacement. (A and B)** Endothelial expression of GFP (left, green), HA-tagged mLRP1 (right, green), and lectin⁺ endothelium (purple) in the cortex of 4-mo-old *Lrp1*$^{lox/lox}$; *Tie2-Cre* mice after AAV2-BR1-*GFP* (left) or AAV2-BR1-m*LRP1* (*LRP1* minigene, right) treatment (A), and quantification of HA-mLRP1⁺ area colocalized with lectin⁺ endothelial capillary profiles (<6 µm in diameter) in the cortex (Ctx) and hippocampus (Hp; B). Scale bar = 25 µm. Mean ± SEM; *n* = 3 mice/group. **(C–E)** IgG (left, purple) and fibrinogen (right, purple) perivascular capillary deposits (C) and quantification (D and E) in 4-mo-old *Lrp1*$^{lox/lox}$; *Tie2-Cre* and *Lrp1*$^{lox/lox}$ mice after AAV2-BR1-*GFP* (top) or AAV2-BR1-m*LRP1* (bottom) treatment. Green, lectin⁺ endothelium. Scale bar = 20 µm. Mean ± SEM, *n* = 14 mice/group. **(F)** High-magnification confocal images from *Lrp1*$^{lox/lox}$; *Tie2-Cre* mouse treated with AAV2-BR1-m*LRP* showing that vessel segments that reexpress HA-mLRP1 (asterisks) were no longer leaky compared with a vessel segment that does not express HA-mLRP1 (arrow) that leaks fibrinogen. Scale bar = 10 µm. **(G–I)** NeuN⁺ neurons and SMI312⁺ neurites (G) and quantification of NeuN⁺ neurons and SMI312⁺ neurites in the cortex and hippocampus of 4-mo-old *Lrp1*$^{lox/lox}$ and *Lrp1*$^{lox/lox}$; *Tie2-Cre* mice after AAV2-BR1-*GFP* (top panels) or AAV2-BR1-m*LRP1* (bottom panels) treatment (H and I). Scale bar = 50 µm. Mean ± SEM, *n* = 14 mice/group. **(J–M)** Burrowing (J), nest

construction (K), novel object location (L), and recognition (M) in 4-mo-old *Lrp1$^{lox/lox}$; Tie2-Cre* and *Lrp1$^{lox/lox}$* mice after AAV2-BR1-*GFP* or AAV2-BR1-m*LRP1* treatment. Mean ± SEM; $n = 14$ mice/group. In B, significance was determined by Student's *t* test. In D, E, and H–M, significance was determined by one-way ANOVA followed by Bonferroni post hoc test. *, $P < 0.05$; **, $P < 0.01$; ***, $P < 0.001$; ****, $P < 0.0001$.

microvessels from *Lrp1$^{lox/lox}$; Tie2-Cre* mice (Fig. 4 G, left), but not in CD13$^+$ pericytes (Fig. 4 G, middle and right). This correlated with elevated *Ppia* (gene encoding CypA) and *Mmp9* mRNA levels in brain endothelial cells, but not in pericytes, from *Lrp1$^{lox/lox}$; Tie2-Cre* mice (Fig. 4 H). Additionally, brain endothelial cells from *Lrp1$^{lox/lox}$; Tie2-Cre* mice compared with control mice had highly elevated gelatinase activity that was inhibited by silencing MMP9 with si.*Mmp9*, but not MMP2 with si.*Mmp2*, confirming that increased gelatinase activity comes from elevated MMP9 (Fig. 4 I).

Inhibition of CypA by short interfering RNA to genetically knock down *Ppia* (Fig. S4 E) or CypA pharmacologic inhibition with cyclosporine A and inhibition of NF-κB with pyrrolidine dithiocarbamate (PDTC) reduced by 75–80% *Mmp9* mRNA (Fig. 3 J) and activated MMP9 levels (Fig. 4 K) in brain endothelial cells from *Lrp1$^{lox/lox}$; Tie2-Cre* mice, suggesting a cell-autonomous NF-κB–dependent transcriptional activation of MMP9 by CypA. Adenoviral-mediated reexpression of m*LRP1* (Ad.m*LRP1*; Fig. S4 F), but not control Ad.*GFP*, restored the ability of murine apoE to transcriptionally suppress *Ppia* (Fig. 4 L) and downstream *Mmp9* mRNA (Fig. 4 M) and active MMP9 levels (Fig. 4 N) in brain endothelial cells from *Lrp1$^{lox/lox}$; Tie2-Cre* mice, indicating that endothelial LRP1 maintains BBB integrity by controlling the CypA–NF-κB–MMP9 pathway, which requires apoE.

To find out whether CypA mediates BBB breakdown in *Lrp1$^{lox/lox}$; Tie2-Cre* mice in vivo, we next performed a proof-of-concept study with cyclosporine A, a pharmacologic inhibitor of CypA, to find out whether CypA inhibition can reverse BBB breakdown in 2-mo-old *Lrp1$^{lox/lox}$; Tie2-Cre* mice. We chose 2-mo-old mice because they develop BBB breakdown at that age but do not have yet neuron loss or behavioral changes. We used a short-term 7-d treatment with low-dose cyclosporine A starting with 10 mg/kg/d for 3 d followed by 5 mg/kg/d for the remaining 4 d, because this short-duration low-dose regimen does not lead to the systemic or central nervous system toxicity frequently seen with longer duration treatments and higher doses of cyclosporine A (see Materials and methods). Additionally, this dosing regimen was previously shown to effectively reverse CypA-driven BBB breakdown in transgenic *APOE4* knockin mice (Bell et al., 2012). Cyclosporine A reduced endothelial CypA and MMP9 levels nearly to the levels seen in *Lrp1$^{lox/lox}$* littermate controls (Fig. S5, A–C), which led to substantial reductions in IgG and fibrin perivascular accumulates in the cortex and hippocampus (Fig. S5, D–F) and recovery of tight junction proteins and collagen IV (Fig. S5 G), suggesting that CypA inhibition can reverse BBB phenotype even in the presence of endothelial LRP1 loss.

Protection from neurodegeneration

Because cyclosporine A is an immunosuppressive CypA inhibitor, we next treated *Lrp1$^{lox/lox}$; Tie2-Cre* mice with a nonimmunosuppressive CypA inhibitor, Debio-025, previously used in patients with hepatitis C (Stanciu et al., 2019) and mouse models of muscular dystrophy and myopathy (Millay et al., 2008; Tiepolo et al., 2009). Debio-025 was initiated in 3-mo-old *Lrp1$^{lox/lox}$; Tie2-Cre* mice at 10 mg/kg/d i.p. for 30 d following previous reports in mouse models of muscular dystrophy and myopathy (Millay et al., 2008; Tiepolo et al., 2009). We started Debio-025 at 3 mo of age, a time point when *Lrp1$^{lox/lox}$; Tie2-Cre* mice have a pronounced BBB breakdown (which we knew could be reversed by CypA inhibition from the cyclosporine A experiment above) and begin developing significant losses of neurons and neuritic density (Fig. S3). The objective of this experiment was to find out whether reversing BBB breakdown with Debio-025 can stop and reverse and/or prevent development of neuron loss and behavioral changes and protect from neurodegeneration that we see in 4-mo-old mice lacking endothelial LRP1.

After 30-d daily treatment with Debio-025, *Lrp1$^{lox/lox}$; Tie2-Cre* mice showed normalized MMP9 levels in the endothelium (Fig. 5, A and B); remarkable reductions in fibrin and IgG extravascular deposits (Fig. 5, C–E); restoration of the tight junction endothelial proteins ZO-1, occludin, and claudin 5 (Fig. 5, F–I); and normalization of BBB permeability to gadolinium, as shown by magnetic resonance imaging (MRI) in the cortex and hippocampus (Fig. 5, J and K). Notably, Debio-025 compared with vehicle protected *Lrp1$^{lox/lox}$; Tie2-Cre* mice against neurodegeneration, as evidenced by increased number of NeuN$^+$ neuron and SMI312$^+$ neuritic density in the cortex and hippocampus nearly to the levels seen in *Lrp1$^{lox/lox}$* littermate controls treated with either Debio-025 or vehicle (Fig. 5, L–N). Compared with vehicle, Debio-025 normalized behavior deficits in *Lrp1$^{lox/lox}$; Tie2-Cre* mice on all four tests close to the levels seen in *Lrp1$^{lox/lox}$* littermate controls treated with vehicle or Debio-025 (Fig. 5, O–R).

Discussion

The present study shows that (1) LRP1 inactivation in the endothelium results in spontaneous disintegration of brain vasculature by activating a self-autonomous CypA–MMP9 BBB-degrading pathway in the endothelium causing loss of key endothelial tight junction proteins (ZO-1, occludin, and claudin 5) and collagen IV, which leads to structural impairment of the BBB; (2) BBB breakdown resulting from loss of brain endothelial LRP1 subsequently leads to loss of neurons and behavioral deficits initiating neurodegenerative process related to leaked blood-derived neurotoxic proteins, e.g., fibrinogen (Cortes-Canteli et al., 2010; Montagne et al., 2018) and others (Bell et al., 2010; Senatorov et al., 2019; Zhao et al., 2015a), as discussed below; (3) brain endothelial–specific in vivo LRP1 gene therapy can reverse vascular phenotype and prevent and reverse neuron loss and behavioral deficits secondary to BBB

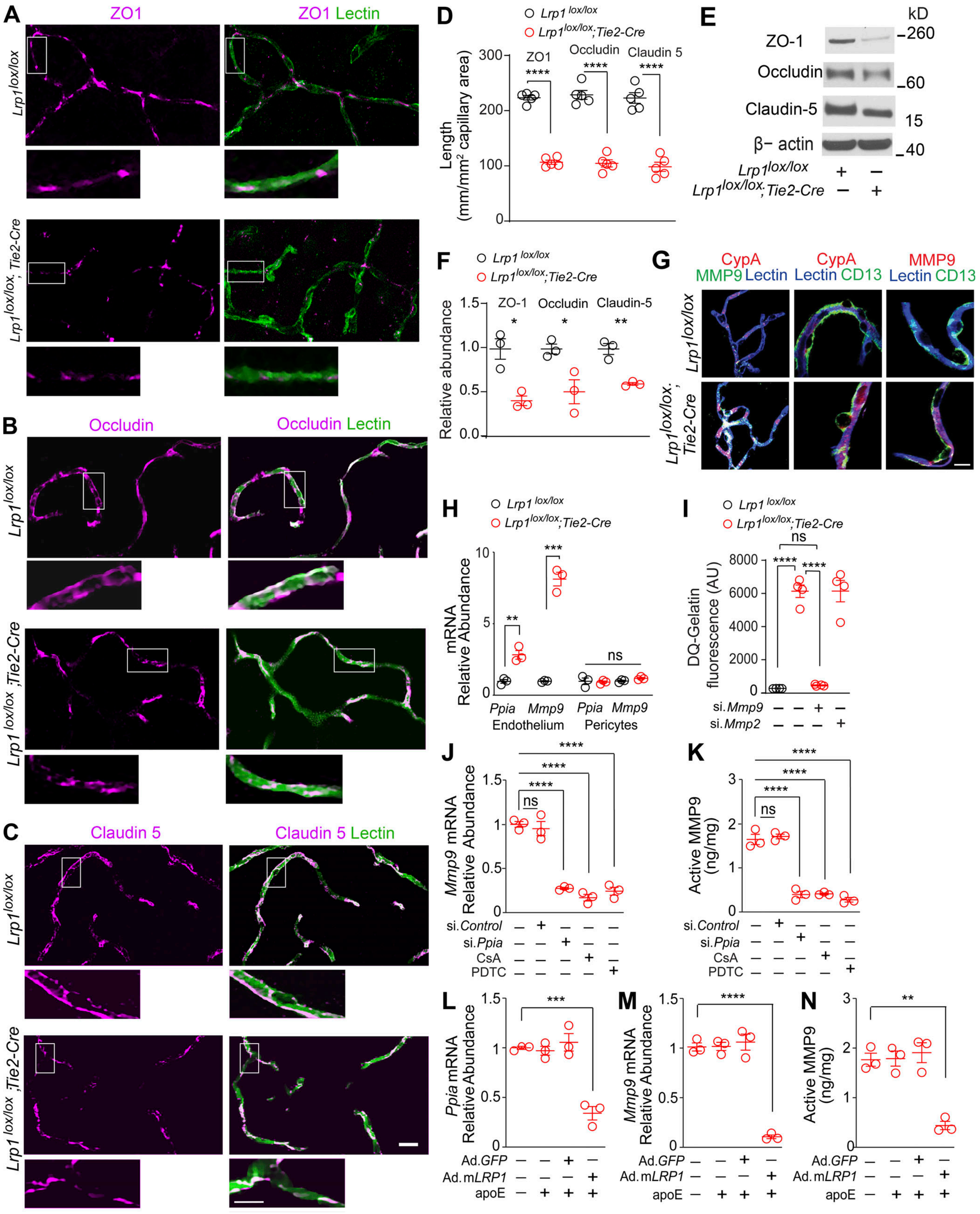

Figure 4. **Activation of CypA-MMP9 pathway after *Lrp1* endothelial loss. (A–D)** ZO-1 (A, purple), occludin (B, purple), and claudin 5 (C, purple) colocalization with endothelial lectin (green) in the cortex of 2-mo-old *Lrp1*$^{lox/lox}$; *Tie2-Cre* mice and *Lrp1*$^{lox/lox}$ controls, and quantification of ZO-1, occludin, and claudin 5 length on lectin^{+} endothelial profiles in these mice (D). Scale bar = 25 µm. Boxes in A–C are sites taken for higher magnification insets shown below single and merged images, scale bar = 10 µm. Mean ± SEM, *n* = 5 mice/group. **(E and F)** Immunoblotting for ZO-1, occludin, and claudin 5 in brain capillaries (E)

and their relative abundance compared with β-actin (F) in *Lrp1*$^{lox/lox}$; *Tie2-Cre* and *Lrp1*$^{lox/lox}$ mice. Mean ± SEM, *n* = 3 mice/group. β-actin, loading control. **(G)** CypA, MMP9, and lectin$^+$ endothelium (left: purple, CypA and lectin; white, MMP9 and lectin); CypA, lectin$^+$ endothelium, and CD13$^+$ pericytes (middle: purple, CypA and lectin), and MMP9, lectin$^+$ endothelium, and CD13$^+$ pericytes (right: purple, MMP9 and lectin) in brain capillaries from *Lrp1*$^{lox/lox}$; *Tie2-Cre* and *Lrp1*$^{lox/lox}$ mice. Scale bar = 10 µm. **(H)** *Ppia* and *Mmp9* mRNA relative abundance normalized to *Gapdh* (housekeeping gene) in brain endothelial cells and pericytes from *Lrp1*$^{lox/lox}$; *Tie2-Cre* and *Lrp1*$^{lox/lox}$ mice. Mean ± SEM, *n* = 5 isolates/group. **(I)** Gelatinase activity in brain endothelial cell medium from *Lrp1*$^{lox/lox}$ and *Lrp1*$^{lox/lox}$; *Tie2-Cre* mice with or without si*Mmp9* or si*Mmp2*. AU, arbitrary units. Mean ± SEM, *n* = 4 isolates/group. **(J and K)** Inhibition of *Mmp9* mRNA (J) and activated MMP9 (K) by CypA silencing (si.*Ppia*), the CypA inhibitor cyclosporine A (CsA; 42 nM), and the NF-κB inhibitor PDTC (20 µM) in brain endothelial cells from *Lrp1*$^{lox/lox}$; *Tie2-Cre* mice. **(L–N)** Inhibition of *Ppia* mRNA (L), *Mmp9* mRNA (M), and active MMP9 (N) in brain endothelial cells from *Lrp1*$^{lox/lox}$; *Tie2-Cre* mice after adenoviral *LRP1* (Ad.m*LRP1*) reexpression in the presence of astrocyte-derived murine apoE (40 nM). Ad*GFP*, control. Mean ± SEM, *n* = 3 isolates/group. All mice were 2 mo old. In D and F, significance was determined by Student's *t* test. In H–N, significance was determined by one-way ANOVA followed by Bonferroni post hoc test. ns, not significant; *, P < 0.05; **, P < 0.01; ***, P < 0.001; ****, P < 0.0001.

---

breakdown; and (4) a nonimmunosuppressive CypA inhibitor, Debio-25, can protect against neurodegeneration even in the presence of LRP1 endothelial deficiency. These new findings complement previously established functions of endothelial LRP1 in regulating clearance of amyloid-β across the BBB (Shibata et al., 2000; Deane et al., 2004; Yamada et al., 2008; Zhao et al., 2015b; Winkler et al., 2015; Storck et al., 2016; Zhu et al., 2018; Shin et al., 2019), angiogenesis in the retina (Mao et al., 2016; Strickland and Muratoglu, 2016), and gene transcription involved in lipid and glucose metabolism (Mao et al., 2017).

Our earlier study (Halliday et al., 2016) showed that CypA and MMP9 levels are increased in brain pericytes and endothelium in postmortem human brain tissue from *APOE4* carriers diagnosed with AD, which was associated with BBB breakdown. This study found that LRP1 levels in blood vessels were greatly reduced in both *APOE4* and *APOE3* AD carriers. However, this study did not show that loss of endothelial LRP1 leads to BBB breakdown, nor did it make the link between loss of endothelial LRP1 and neurodegeneration and neuron loss. Another earlier study by our group (Bell et al., 2012) showed that the *APOE* gene controls cerebrovascular integrity in mice by regulating CypA expression in pericytes. Using *APOE* transgenic mice, this earlier study demonstrated that *APOE4*, but not *APOE3*, leads to activation of the CypA–MMP9 pathway in pericytes in the presence of normal levels of LRP1. This in turn leads to BBB breakdown, followed by changes in the cortical activity determined by voltage-sensitive dye imaging. However, whether *APOE4* transgenic mice develop neuron loss and/or behavioral changes has not been studied, and neither has the role of endothelial LRP1 in maintaining the BBB and/or neuronal functions. In contrast, the present study using an endothelial LRP1 knockout line, brain endothelial–specific gene therapy with LRP1, and pharmacological treatment with a nonimmunosuppressive CypA inhibitor targeting the BBB endothelium has established the link between loss of endothelial LRP1, neurodegeneration, and behavior, which has not been studied by these earlier reports.

A number of different LRP1 ligands, including apoE, α2-macroglobulin (α2M), and others, might be affected by LRP1 endothelial inactivation. Since LRP1 is substantially reduced in blood vessels in AD (Shibata et al., 2000; Deane et al., 2004; Zhao et al., 2015b; Winkler et al., 2015; Donahue et al., 2006; Halliday et al., 2016; Jaeger et al., 2009), its inactivation could potentially lead to activation of the CypA–MMP9 pathway not only by apoE4, as in *APOE4* transgenic mice (Bell et al., 2012) and human *APOE4* carriers (Montagne et al., 2020), but also by apoE3, which requires intact LRP1 to suppress this pathway (Bell et al., 2012). Additionally, LRP1 endothelial loss may affect clearance of soluble Aβ across the BBB either alone or complexed with apoE and/or α2M, leading to retention of apoE-Aβ and α2M-Aβ complexes in the brain. Excess Aβ, on the other hand, reduces LRP1 levels in the brain endothelium by accelerating its proteasome-dependent degradation (Deane et al., 2004), which in turn can accelerate both Aβ-dependent and Aβ-independent pathways of neurodegeneration. Besides these potential effects of LRP1 endothelial deficiency, LRP1 global deficiency inhibits Aβ generation and simultaneously impairs Aβ clearance, implicating a more complex role for LRP1 than in BBB regulation alone (Van Gool et al., 2019).

LRP1 also interacts with different membrane receptors, such as Wnt receptor frizzled 1 (Zilberberg et al., 2004) and Notch3 (Meng et al., 2010), and therefore, its inactivation may disrupt these signaling pathways. Interestingly, when subjected to a high-fat diet, mice with endothelial-specific *Lrp1* deletion display a reduction in body weight, but when fed a normal chow diet, they do not lose weight (Mao et al., 2017), as we also observed.

The present study did not find developmental changes in the BBB in mice after endothelial-specific *Lrp1* deletion. Why the BBB remains intact shortly after birth remains presently unclear. It is possible, however, that there is an age-related change in a key circulating or cell-autonomous gene that initiates the BBB deficits at ~1–2 mo of age, or it could be microbiome related due to changes in gut microbiome after birth. Future studies should explore these possibilities. Our data also show that BBB breakdown in mice born with endothelial-specific *Lrp1* deletion occurs at 1–2 mo of age, which precedes neuronal changes that are seen for the first time at 3 mo of age. However, it is possible that deficient neurovascular coupling after 3 mo of age when neuronal changes develop might leave active microvascular regions more vulnerable to loss of endothelial LRP1, which can contribute to accelerated BBB injury, as we see in mice with endothelial-specific *Lrp1* deletion at an older age of 4 mo.

Finally, we would like to comment that ~20 studies suggested expression of LRP1 in brain endothelial cells based on immunostaining, Western blotting, and/or immunogold electron microscopy in mice, rats, humans, bovines, and porcine models (Shibata et al., 2000; Deane et al., 2004; Yamada et al., 2008; Zhao et al., 2015b; Winkler et al., 2015; Storck et al., 2016; Zhu et al., 2018; Shin et al., 2019; Mao et al., 2016; Strickland and

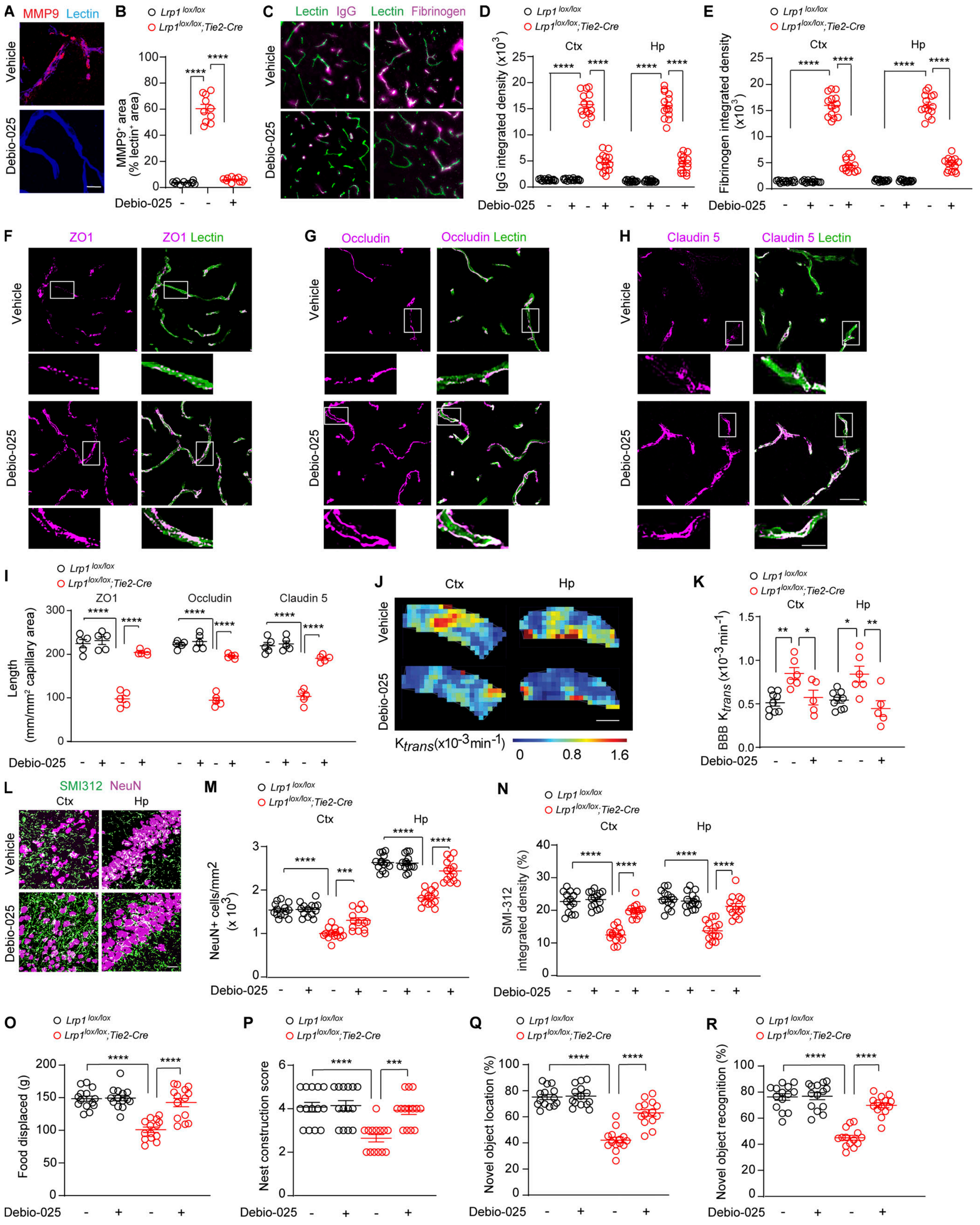

Figure 5. **Cyclophilin A inhibitor Debio-025 reverses vascular phenotype and protects from neurodegeneration in *Lrp1*$^{lox/lox}$; *Tie2-Cre* mice. (A and B)** MMP9 immunoreactivity in cortical endothelium (A) and quantification (B) in *Lrp1*$^{lox/lox}$; *Tie2-Cre* mice after vehicle or Debio-025 treatment. Scale bar = 10 µm. Mean ± SEM, *n* = 10 mice/group. **(C–E)** IgG and fibrin deposits in the cortex (C) and quantification of their deposits in the cortex (Ctx) and hippocampus (Hp; D

and E) in *Lrp1*$^{lox/lox}$ and *Lrp1*$^{lox/lox}$; *Tie2-Cre* mice after vehicle or Debio-025 treatment. Scale bar = 20 µm. Mean ± SEM, *n* = 14 mice/group. **(F–I)** ZO-1 (F, purple), occludin (G, purple), and claudin 5 (H, purple) colocalization with endothelial lectin (green) in the cortex of 4-mo-old *Lrp1*$^{lox/lox}$; *Tie2-Cre* mice treated with vehicle or Debio-25, and quantification of ZO-1, occludin, and claudin 5 length on lectin$^+$ endothelial capillary profiles in these mice (I). Scale bar = 25 µm. Boxes in F–H are sites taken for higher magnification insets shown below single and merged images. Scale bar = 10 µm. White (merged), colocalization of ZO-1, occludin, or collagen with lectin. Mean ± SEM, *n* = 5 mice/group. **(J and K)** BBB K_{trans} maps (J) and K_{trans} values in the cortex and hippocampus (K) in *Lrp1*$^{lox/lox}$; *Tie2-Cre* mice after vehicle or Debio-025 treatment, compared with *Lrp1*$^{lox/lox}$ mice treated with vehicle. Scale bar = 0.5 mm. Mean ± SEM, *n* = 5–6 mice/group. **(L–N)** NeuN$^+$ neurons and SMI312$^+$ neurites (L) and quantification of NeuN$^+$ neurons and SMI312$^+$ neurites in the cortex and hippocampus (M and N) in 4-mo-old *Lrp1*$^{lox/lox}$ and *Lrp1*$^{lox/lox}$; *Tie2-Cre* mice after vehicle or Debio-025 treatment. Scale bar = 50 µm. Mean ± SEM, *n* = 14 mice/group. **(O–R)** Burrowing (O), nest construction (P), novel object location (Q), and recognition (R) in *Lrp1*$^{lox/lox}$ and *Lrp1*$^{lox/lox}$; *Tie2-Cre* mice after vehicle or Debio-025 treatment. Mean ± SEM, *n* = 14 mice/group. All mice were 4 mo old. Debio-025 (10 mg/kg/d) or vehicle were given for 30 d starting at 3 mo of age. In B, significance was determined by Student's *t* test. In D, E, I, K, and M–R, significance was determined by one-way ANOVA followed by Bonferroni post hoc test. *, P < 0.05; **, P < 0.01; ***, P < 0.001; ****, P < 0.0001.

Muratoglu, 2016; Donahue et al., 2006; Halliday et al., 2016; Jaeger et al., 2009; Wang et al., 2003; Demeule et al., 2008; Ueno et al., 2010; Pflanzner et al., 2011; Gali et al., 2019; Wu et al., 2020). Four studies using endothelial-specific *Lrp1* knockout mice have shown striking pathophysiological consequences of LRP1 endothelial inactivation, including accumulation of Aβ pathology (Storck et al., 2016), regulation of angiogenesis (Mao et al., 2016), gene transcription (Mao et al., 2017), and, presently, BBB breakdown and neurodegeneration. We also showed in the present study by immunoblotting, quantitative real-time PCR, and immunostaining that LRP1 is expressed in brain endothelium in control mice. RNA sequencing (RNA-seq) studies using bulk RNA-seq in mouse brain endothelial RiboTag-isolated cells (Jambusaria et al., 2020) and human brain endothelial cells (Zhang et al., 2016), and single-cell RNA-seq studies in mouse brain endothelial cells (Zeisel et al., 2015; Sabbagh et al., 2018), confirmed expression of *Lrp1* in mice and *LRP1* in humans at a moderate number of copies but comparable to those found in neurons, microglia, or oligodendrocytes. Other single-cell RNA-seq studies of mouse endothelial cells showed a low to high number of *Lrp1* copies depending on the brain endothelial cell subtype (Zeisel et al., 2018), a very low number of copies and absence from some cells (Vanlandewijck et al., 2018), or even complete absence (Kalucka et al., 2020). The reasons for the discrepancies between different types of RNA-seq studies remain unclear at present. However, they could be attributed to the differences in the methods used, type of tissue and cell collection, number of cells analyzed, and/or number of reads. Additionally, it is worth mentioning that the steady-state levels of proteins may or may not reflect rates of transcription. For example, a comparison of subunit stoichiometry and ribosome profiling versus RNA-seq reads has shown that RNA does not reflect at all subunit stoichiometry, while the translational landscape does (Li et al., 2014).

In summary, we show that endothelial LRP1 protects BBB integrity and the brain against neurodegeneration by suppressing CypA activation in the endothelium. This is of particular interest for neurodegenerative disorders associated with vascular dysfunction and cognitive decline and loss of endothelial LRP1, such as AD (Sweeney et al., 2018). Previous studies have shown that BBB breakdown leads to leakages into brain parenchyma of several neurotoxic blood-derived proteins, such as albumin (Senatorov et al., 2019), thrombin, plasminogen and/or iron-containing proteins (Bell et al., 2012, 2010), or fibrinogen (Cortes-Canteli et al., 2010; Montagne et al., 2018), that all can initiate neurodegenerative changes and neuron loss by different but complementary mechanisms. The present study also shows that endothelial LRP1 gene replacement therapy or CypA inhibition in the presence of endothelial LRP1 loss can reverse vascular phenotype and prevent and/or reverse development of neurodegenerative changes. These findings have implications both for the pathophysiology and treatment of neurodegeneration linked to vascular dysfunction.

Materials and methods

Animals

Mice were housed in plastic cages on a 12-h light cycle with ad libitum access to water and a standard laboratory diet. All procedures were approved by the Institutional Animal Care and Use Committee at the University of Southern California with National Institutes of Health guidelines. *Lrp1*$^{lox/lox}$ mice were kindly provided by Dr. J. Herz at UT Southwestern Medical Center (Dallas, TX; Boucher et al., 2003) and crossed with an endothelial-specific *Tie2-Cre* line (Kisanuki et al., 2001) to generate *Lrp1*$^{lox/lox}$; *Tie2-Cre* mice with endothelial-specific LRP1 deletion. All animals were genotyped by PCR using protocols and primer sequences as described by the distributor or donating investigator. Animals of both sexes at P8 and 2 and 4 mo of age were used in the experiments. All animals were included in the study. All animals were randomized for their genotype information. All experiments were blinded; the operators responsible for the experimental procedures and data analysis were blinded and unaware of group allocation throughout the experiments.

Treatments

Brain endothelial cell–specific AAV2-BR1-mLRP1 therapeutic vector

For the rescue experiment, 3-mo-old *Lrp1*$^{lox/lox}$*; Tie2-Cre* mice were administered intravenously with adeno-associated AAV2-BR1-m*LRP1* vector or AAV2-BR1-*GFP* control construct. We chose to treat 3-mo-old *Lrp1*$^{lox/lox}$*; Tie2-Cre* mice, because at this age, these mice develop a pronounced BBB breakdown and moderate but significant neuronal damage. To this end, the previously reported *LRP1* minigene (m*LRP1*) containing the LRPIV extracellular domain and the intracellular cytoplasmic domain of the human *LRP1* gene (Bell et al., 2012; Zhao et al., 2015b) was packaged into brain microvascular endothelial-specific AAV2-BR1 vector particles (Körbelin et al., 2016). Surgical procedures were performed under general anesthesia with isoflurane (1–1.5%) using the SomnoSuite Small Animal Anesthesia System (Kent Scientific). Rectal temperature was monitored and maintained at 36.5 ± 0.5°C. AAV2-BR1-m*LRP1* or AAV2-BR1-*GFP* constructs were injected through the tail vein at a dose of 2×10^{11} gp/mouse that has been shown previously to lead to a successful gene transfer to the brain endothelia with AAV2-BR1 serotype (Körbelin et al., 2016). Tissue and behavior analyses were performed at 4 mo of age.

Cyclosporine A proof-of-concept study

First, we performed a proof-of-concept study with cyclosporine A (Sadimmune, 50 mg/ml, dissolved in sterile 0.9% saline; Novartis), a pharmacologic inhibitor of CypA, to find out whether CypA inhibition can reverse BBB breakdown in 2-mo-old *Lrp1*$^{lox/lox}$; *Tie2-Cre* mice. We chose 2-mo-old mice because they develop BBB breakdown but do not yet have neuronal loss or behavioral changes. We used a short-term 7-d treatment with low-dose cyclosporine A starting with 10 mg/kg/d for 3 d followed by 5 mg/kg/d for the remaining 4 d, because it has been previously shown that this short-duration low-dose regimen (1) does not lead to systemic or central nervous system toxicity frequently seen with longer duration treatments and with higher doses of cyclosporine A (Famiglio et al., 1989; Santos and Schauwecker, 2003; Lim et al., 2013) and (2) effectively reverses CypA-driven BBB breakdown in transgenic *APOE4* knockin mice (Bell et al., 2012).

Treatment with Debio-025

Because cyclosporine A is an immunosuppressive CypA inhibitor, we next studied Debio-025 (catalog number HY-12559; MedChem Express), a nonimmunosuppressive CypA inhibitor that has been used in humans for nonneurological indications such as hepatitis C (Stanciu et al., 2019). Debio-025 was initiated in 3-mo-old *Lrp1*$^{lox/lox}$; *Tie2-Cre* mice at 10 mg/kg/d i.p. for 30 d following previous reports in mouse models of muscular dystrophy and myopathy (Millay et al., 2008; Tiepolo et al., 2009). We started Debio-025 at 3 mo of age, when *Lrp1*$^{lox/lox}$; *Tie2-Cre* mice have a pronounced BBB breakdown (which we knew could be reversed by CypA inhibition from the cyclosporine A experiment) and moderate but significant loss of neurons and neuritic density. The objective of this experiment was to find out whether reversing BBB breakdown with Debio-025 can prevent development of neuron loss and behavioral changes that we see in 4-mo-old mice lacking endothelial LRP1.

In vitro studies

Isolation of brain capillaries

Brain capillaries were isolated using dextran gradient centrifugation followed by sequential cell-strainer filtrations, as we have previously described (Bell et al., 2012). Briefly, cerebral cortices devoid of cerebella, white matter, and leptomeninges were prepared and cut into small pieces in ice-cold PBS containing 2% FBS and then homogenized by a Dounce tissue grinder (0.25 mm clearance) with approximately five strokes. Dextran (70 kD; Sigma) was subsequently added to yield a final concentration of 16%, and the samples were thoroughly mixed. The samples were then centrifuged at 6,000 *g* for 15 min. The microvessel-depleted brain (brain tissue minus capillaries) remained on top of the dextran gradient, and the capillary pellet located at the bottom of the tubes was collected and sequentially filtered through a 100-µm and 45-µm cell strainer (BD Falcon). The capillaries remaining on top of the 45-µm cell strainer were collected in PBS and lysed for immunoblot analysis, cytospun for immunofluorescent staining analysis, or processed to establish primary endothelial and pericyte cell cultures as described below.

Brain endothelial cell culture

Primary mouse brain endothelial cells were isolated and cultured as we and others previously described (Zhao et al., 2015b; Ruck et al., 2014). Briefly, isolated brain microvessels were resuspended in 9 ml DMEM plus 1 ml collagenase/dispase (final concentration is 1 mg/ml) and 0.1 ml DNase I (1 mg/ml in PBS) and digested for 1 h at 37°C on an orbital shaker at 180 rpm. The cells were centrifuged at 1,000 *g* for 12 min, and the pellet was resuspended in 10 ml of complete culture medium (catalog number M1168; Cell Biologics; containing 5% FBS, 1% nonessential amino acids, 1% vitamins and endothelial cell growth supplement comprising vascular endothelial growth factor, heparin, and epidermal growth factor), plated in a T25 tissue culture flask precoated with collagen IV (0.4 mg/ml) and 100 µl fibronectin (0.1 mg/ml), and cultured at 37°C with 5% CO_2 in a humidified incubator. After 6–12 h, the nonadherent cells were rinsed away, and fresh medium was replaced every 2–3 d until the cell population became confluent. Cultures were confirmed to be morphologically consistent with primary endothelial cultures with cobblestone-like shape and positive for endothelial markers, including von Willebrand factor, CD31, and vascular endothelial–cadherin. Cultures were negative for the pericyte markers PDGFRβ, CD13, and NG2; vascular smooth muscle cell markers, including α-smooth muscle actin; the astrocyte markers GFAP and AQP4; the neuronal markers MAP2 and NeuN; and the microglia marker Iba1, as we previously reported (Bell et al., 2012; Zhao et al., 2015b). siRNA transfections were performed using Lipofectamine RNAiMAX Reagent (Thermo Fisher Scientific) following the manufacturer's instructions, as we previously reported (Zhao et al., 2015b).

Adenoviral-mediated reexpression of mLRP1 in brain endothelial cells

In a subset of experiments, primary brain endothelial cells isolated from 2-mo-old *Lrp1*$^{lox/lox}$; *Tie2-Cre* mice were placed in 12-well plates and incubated with Ad.m*LRP1* or Ad.*GFP* adenovirus at concentration of 10^7 PFU/ml. Cells were harvested 72 h after virus transduction for LRP1 minigene Western blot analysis using anti-HA tag antibody (catalog number 372S; Cell Signaling Technology).

DQ-gelatin degradation assay

The gelatinolytic activity of matrix metalloproteases was determined in the conditioned medium from brain endothelial cell cultures from 2-mo-old *Lrp1*$^{lox/lox}$; *Tie2-Cre* mice and *Lrp1*$^{lox/lox}$ littermate controls using DQ-Gelatin (D-12054; Invitrogen) assay as reported (Vandooren et al., 2011). Four independent primary mouse brain endothelial cell cultures (200,000 cells/well, four wells per culture) were used for all studied conditions. For MMP2 and MMP9 knockdown, Accell *Mmp2* siRNA (E-047467-00-0010; Dharmacon) and Accell *Mmp9* siRNA (E-065579-00-0010; Dharmacon) at a final concentration of 1 µM in Accell siRNA Delivery Media (B-005000-500; Dharmacon) were added into 90% confluent cultures and incubated for 72 h. The conditioned medium was then collected, centrifuged, and incubated with DQ-Gelatin in a 96-well plate, and the fluorescence was measured at 485/530-nm excitation/emission wavelengths using a fluorescence reader (Victor 3; Perkin Elmer).

Active MMP9

Active MMP9 was determined in brain endothelial cell cultures using a previously described method (Aleksinskaya et al., 2013). Briefly, primary brain endothelial cells from 2-mo-old *Lrp1*$^{lox/lox}$; *Tie2-Cre* mice with silenced CypA (si.*Ppia*) or si.*Control*, in the presence of the CypA inhibitor cyclosporine A and the NF-κB inhibitor PDTC, and after adenoviral *LRP1* (Ad.m*LRP1*) re-expression or control Ad.*GFP* in the presence of astrocyte-derived murine apoE, were harvested for mouse MMP9 activity assay (QuickZyme). MMP9 was captured by a mouse-specific antibody, and its activity was detected based on cleavage of chromogenic substrates as measured at 405 nm using an ELISA plate reader.

Brain pericyte culture

Primary mouse brain pericytes were isolated for in vitro culturing as we previously described (Sagare et al., 2013). Briefly, isolated microvessel fragments were digested for 12 h at 37°C with collagenase A (10103586001; Roche) with constant shaking and vigorous pipetting every 3–4 h. The cells were then spun down and washed with PBS and then plated in complete medium containing DMEM, 10% FBS, 1% nonessential amino acids, 1% vitamins, and 1% antibiotic/antimycotic on plastic (noncoated) tissue culture plates. After 6–12 h, the nonadherent cells were rinsed away, and fresh medium was replaced every 2–3 d. Cultures were confirmed to be morphologically consistent with pericyte cultures and were positive for the pericyte markers PDGFRβ, CD13, NG2, and desmin. Cultures were negative for the endothelial markers von Willebrand factor and CD31, the astrocyte markers GFAP and AQP4, the neuronal markers MAP2 and NeuN, and the microglia marker Iba1, as we previously reported (Bell et al., 2012).

Western blotting

All samples (isolated brain capillaries, endothelial cells, and pericytes) from Lrp1lox/lox; Tie2-Cre mice and Lrp1lox/lox littermate controls were lysed in RIPA buffer (50 mM Tris, pH 8.0, 150 mM NaCl, 0.1% SDS, 1.0% NP-40, 0.5% sodium deoxycholate, and protease inhibitor cocktail; Roche). Samples were then subjected to SDS-Page gel electrophoresis and transferred to a nitrocellulose membrane. Membranes were blocked with 5% milk, incubated with the following primary antibodies: rabbit anti–ZO-1 (catalog number 40–2200, 1:1,000; Invitrogen), rabbit anti-occludin (catalog number16453, 1:500; BD Biosciences), rabbit anti-claudin-5 (catalog number ab15106, 1:1,000; Abcam), rabbit anti–GLUT-1 (CBL242, 1:500; Millipore), and rabbit anti-human MFSD2A (catalog number A18288, 1:1,000; ABclonal). They were then incubated with HRP-conjugated donkey anti-rabbit secondary antibody (catalog number A16029, 1:5,000; Invitrogen). Membranes were then treated with SuperSignal West Pico PLUS chemiluminescent substrate (Thermo Fisher Scientific). For Fig. 1, A and D, we used a digital chemiluminescence imaging system (ChemiDoc MP, Universal Hood III; Bio-Rad) to capture images as .tiff files using Image Lab 6.0.1 software. For all other figures, treated membranes were exposed to CL-XPosure film (Thermo Fisher Scientific) and developed in a X-OMAT 3000 RA film processor (Kodak) or ChemiDoc XRS system from Bio-Rad.

RNA extraction and quantitative real-time PCR

RNA extraction from brain endothelial cells and pericyte cultures from *Lrp1*$^{lox/lox}$; *Tie2-Cre* mice and *Lrp1*$^{lox/lox}$ littermate controls was performed using the SV Total RNA Isolation kit (catalog number Z3100; Promega) following the manufacturer's instructions. 100 ng total RNA was used as template for quantitative real-time PCR, and amplification was performed using qScript One-Step quantitative real-time PCR kit (catalog number 95057–050; Quanta Biosciences). To examine mRNA expression of *Lrp1* (forward: 5′-ACTATGGATGCCCCTAAAACTTG-3′, reverse: 5′-GCAATCTCTTTCACCGTCACA-3′) and *Gapdh* (forward: 5′-AGGTCGGTGTGAACGGATTTG-3′, reverse: 5′-TGTAGACCA TGTAGTTGAGGTCA-3′), specific forward and reverse primers were used. Data were analyzed by normalizing the expression of *Lrp1* to *Gapdh* (housekeeping gene) within endothelial cells and pericytes. For relative gene expression calculations, we used the 2^(−ΔCt) method, where Ct (cycle threshold) is defined as the number of cycles required for the fluorescent signal to cross the threshold (i.e., exceeds background level). With respect to the ΔCt of the 2^(−ΔCt) method, ΔCt is the difference in the threshold cycles between *Lrp1* and *Gapdh* genes.

Immunohistochemistry

Animals were anesthetized with an i.p. injection of 100 mg/kg ketamine and 10 mg/kg xylazine and transcardially perfused first with 15 ml saline, followed by 20 ml of 4% paraformaldehyde (PFA) in PBS. Brains were removed and postfixed overnight with 4% PFA at 4°C before brain sections were cut at 30 µm thickness. Retinas from P8 mice were processed as previously described (Trost et al., 2013). Cytospins from isolated microvessels were fixed with 4% PFA for 10 min at room temperature and subsequently washed three times in PBS. Tissue sections were blocked with 5% normal donkey serum (Vector Laboratories)/0.1% Triton-X/0.01 M PBS and incubated with primary antibodies diluted in blocking solution overnight at 4°C. All primary and secondary antibodies are listed in Table S1. To visualize brain microvessels, sections were incubated with Dylight 488–, 594–, or 647–conjugated *L. esculentum* lectin (Vector Laboratories) as we have previously reported (Zhao et al., 2015b; Bell et al., 2010). After incubation with primary antibodies, sections were washed in PBS and incubated with fluorophore-conjugated secondary antibodies (see Table S1) and then mounted onto slides with DAPI fluorescence mounting medium

(Dako). Sections were imaged with a Zeiss LSM 510 confocal laser-scanning microscope using a series of high-resolution optical sections (1,024 × 1,024-pixel format) that were captured with a 25× water-immersion objective with 1× zoom at 1-µm step intervals for z-stacks. Laser settings for gain, digital offset, and laser intensity were kept standardized between different treatments and experiments. Z-stack projections and pseudocoloring were performed using ZEN software (Carl Zeiss Microimaging). Postanalysis imaging was performed using ImageJ software.

Quantification analysis

For quantification of extravascular leakages, NeuN$^+$ neuronal nuclei, neurofilament SMI-312$^+$ axons, tight junction protein, and collagen IV length, pericyte, aquaporin-4, and syntrophin coverages of brain capillary lectin$^+$ endothelial profiles (microvessels <6 µm in diameter), CypA, MMP9, and HA-mLRP1 immunoreactivity in brain capillary (<6 µm in diameter) lectin$^+$ endothelium, four to six randomly selected fields per animal in the somatosensory cortex region and/or CA1 region of the hippocampus were analyzed in three or four nonadjacent sections (~100 µm apart) and averaged per mouse. The image area analyzed was 640 × 480 µm. The number of animals used for each analysis is indicated in the respective figure legends.

Extravascular leakages

Blood-derived fibrin(ogen) and IgG perivascular capillary deposits in the cortex and hippocampus were quantified as we previously described (Sagare et al., 2013; Bell et al., 2010; Winkler et al., 2015). Briefly, for quantification of extravascular fibrinogen deposits, an antibody that detects both fibrinogen and fibrinogen-derived fibrin polymers was used. 10-µm maximum projection z-stacks were reconstructed, and the fibrinogen extravascular signal on the abluminal side of lectin$^+$ endothelial profiles on brain capillaries (<6 µm in diameter) was analyzed using ImageJ (Bell et al., 2010). A similar approach was used to quantify IgG deposits.

NeuN$^+$ neuronal nuclei

10-µm maximum projection z-stacks were reconstructed, and NeuN$^+$ neurons in the cortex and hippocampus were quantified using the ImageJ Cell Counter analysis tool as we previously described (Bell et al., 2010; Nikolakopoulou et al., 2019).

Neurofilament SMI-312$^+$ axons

As we previously described (Bell et al., 2010; Nikolakopoulou et al., 2019), 10-µm maximum projection z-stacks were reconstructed, and SMI-312$^+$ signal in the cortex and hippocampus was subjected to threshold processing and analyzed using ImageJ. The areas occupied by the signal were then analyzed using the ImageJ area measurement tool. Total SMI-312$^+$ area was expressed as a percentage of total brain area in each field.

Tight junction proteins and collagen IV

The length of ZO-1$^+$, occludin$^+$, and claudin 5$^+$ immunofluorescent signals on lectin$^+$ endothelial brain capillary profiles (<6 µm in diameter) in the cortex was determined using the ImageJ area measurement tool and expressed in millimeters of ZO-1, occludin, and claudin 5 length per square millimeter of the area of brain capillary lectin$^+$ endothelial profiles (<6 µm in diameter). A similar approach was used to quantify collagen IV length.

Pericyte coverage of brain capillaries

10-µm maximum projection z-stacks were reconstructed, and the areas occupied by CD13$^+$ pericyte on brain capillary lectin$^+$ endothelial profiles (<6 µm in diameter) were analyzed using ImageJ as we previously described (Nikolakopoulou et al., 2017).

Astrocyte coverage of brain capillaries with aquaporin 4

10-µm maximum projection z-stacks were reconstructed, and the areas occupied by aquaporin 4$^+$ astrocyte endfeet on brain capillary lectin$^+$ endothelial profiles (<6 µm in diameter) were analyzed using ImageJ as we previously described (Nikolakopoulou et al., 2019).

Astrocyte coverage of brain capillaries with syntrophin

10-µm maximum projection z-stacks were reconstructed, and the areas occupied by syntrophin$^+$ astrocyte endfeet on brain capillary lectin$^+$ endothelial profiles (<6 µm in diameter) were analyzed using ImageJ as we previously described (Nikolakopoulou et al., 2019).

CypA endothelial immunofluorescent detection

The CypA$^+$ area occupying brain capillary lectin$^+$ endothelial profiles (microvessels <6 µm in diameter) was determined using immunofluorescent detection and expressed as a percentage of brain capillary lectin$^+$ endothelial area using the ImageJ area measurement tool as we previously described (Bell et al., 2012).

MMP9 endothelial immunofluorescent detection

The MMP9$^+$ area occupying brain capillary lectin$^+$ endothelial profiles (microvessels <6 µm in diameter) was determined using immunofluorescent detection and expressed as a percentage of brain capillary lectin$^+$ endothelial area using the ImageJ area measurement tool as we previously described (Bell et al., 2012).

HA-mLRP1 expression in endothelium after AAV2-BR1-mLRP1 treatment

The HA-mLRP1$^+$ area occupying brain capillary lectin$^+$ endothelial profiles (microvessels <6 µm in diameter) in *Lrp1*$^{lox/lox}$; *Tie2-Cre* mice after AAV2-BR1-m*LRP1* treatment was expressed as a percentage of brain capillary lectin$^+$ endothelial area using the ImageJ area measurement tool as we previously described (Bell et al., 2012).

Microvascular length and branching points

Total length and branching points of microvessels (<6 µm in diameter) were manually quantified using ImageJ plugins, including NeuronJ for microvessel length and Cell Counter for branching points, and expressed as per square millimeter of tissue, as previously reported (Ma et al., 2013).

LRP1 endothelial expression in freshly isolated brain capillaries

Triple immunostaining for LRP1 (rabbit anti-human LRP1 [EPR3724], ab92544; 1:100; Abcam), CD13 (AF2335; 1:100; R&D Systems) for pericytes, and the endothelial-specific markers CD31 (550274; 1:100; BD PharMingen) or GLUT1 (Alexa Fluor 594–conjugated, ab206360; 1:200; Abcam) was performed on isolated brain capillaries (cytospins) from *Lrp1*$^{lox/lox}$ control mice and *Lrp1*$^{lox/lox}$*; Tie2-Cre* mice to confirm LRP1 expression in brain capillary endothelium in control mice and its deletion from endothelium in LRP1 endothelial-specific knockout mice. Secondary antibodies were Alexa Fluor 488–conjugated donkey anti-rabbit (A-21206; 1:500; Invitrogen) for LRP1-positive cells, Alexa Fluor 594–conjugated goat anti-rat (A-11007; 1:500; Invitrogen) for CD31^{+} endothelium, and Alexa Fluor 647–conjugated donkey anti-goat (A-21447; 1:500; Invitrogen) for CD13^{+} pericytes. Orthogonal projection views of confocal images of LRP1 with endothelial marker CD31 showing expression of LRP1 in brain capillary endothelium in *Lrp1*$^{lox/lox}$ control mice, and loss of LRP1 from endothelium in brain capillaries from *Lrp1*$^{lox/lox}$*; Tie2-Cre* mice, were generated from 20 single-plane maximum projection intensity z-stacks using ImageJ.

Brightfield microscopy

Prussian blue staining was performed using the Iron Stain Kit (HT-20) per the manufacturer's instructions, as we previously described (Bell et al., 2012, 2010). For quantification of Prussian blue–positive hemosiderin deposits, a minimum of six nonadjacent coronal cortical sections (~100 µm apart) per mouse were analyzed. The mean number of Prussian blue–positive hemosiderin deposits per animal was expressed per square millimeter of tissue. For counterstain, sections were stained with Cresyl Violet per the manufacturer's instructions (Cresyl Violet Stain Solution, 0.1%, ab246816; Abcam).

Cranial window

Animals were initially anesthetized with 100 mg/kg ketamine and 10 mg/kg xylazine and placed on a heating pad (37°C). The cranium of the mouse was firmly secured in a stereotaxic frame (Kopf Instruments). A high-speed dental drill (tip FST 19007-05; Fine Science Tools) was used to thin a cranial window ~5 mm in diameter over the somatosensory cortex, and 45° forceps were used to remove the piece of skull. Gelfoam (Pharmacia & Upjohn) was applied immediately to control any cranial or dural bleeding. A sterile 5-mm glass coverslip was then placed on the dura mater and sealed with cyanoacrylate-based glue.

In vivo two-photon imaging of BBB permeability to FITC-dextran

For BBB permeability measurements of FITC-dextran (40 kD) leakage from cortical microvessels, mice were anesthetized with isoflurane, fixed in a stereotaxic frame (Kopf Instruments) under a two-photon microscope (with 20×, 1.0 NA objective), and maintained at 1.2% isoflurane throughout the experiment. Body temperature was maintained at 37°C with a homeothermic heating pad. In vivo images were acquired using a custom-built Zeiss LSM 5MP multiphoton microscope coupled to a mode locked Ti/sapphire laser (Mai Tai Deep See; Spectra Physics) set to 800 nm. FITC emission was collected using a 500–550 nm bandpass filter. Immediately before image acquisition, the vasculature was labeled via retro-orbital injection of 40 kD FITC-dextran dye (0.1 ml of 10 mg/ml: Thermo Fisher Scientific). FITC-dextran–labeled vasculature and diffusion (leakage) of FITC-dextran from cortical capillaries into the parenchyma was imaged through the cranial window every 5 min for 30 min. The imaging depth was 200 µm, and the images acquired did not include pial vessels. Leaky microvessels were mainly capillaries with a diameter <6 µm. The acquired images (see Fig. 1 D) were not 3D reconstructions of z-stacks. These were single focal planes. In this case, the thickness of image volume depends on point-spread function (effectively the focal volume) in the z direction of the excitation laser, which is ~1 µm for the two-photon imaging system used.

Calculation of the BBB permeability–surface area product

Data were analyzed as previously reported using a slightly modified approach (Bell et al., 2010). Time series image stacks were registered (StackReg, ridged body algorithm) in FIJI (ImageJ; Schindelin et al., 2012), and an ~400 × 400-µm region of interest (ROI) was selected from the image sequence for analysis. To determine the fluorescence in the parenchyma over time, a mask of the vessels in the ROI was made using the Huang threshold setting in FIJI, and the resulting binary mask was subtracted from the original ROI image sequence.

The in vivo BBB permeability for FITC-dextran was estimated as the permeability–surface area product (PS) as we previously described (Bell et al., 2010; Nikolakopoulou et al., 2019; Deane et al., 2003) using the following formula:

$$\mathrm{PS} = \frac{(1-\mathrm{Hct})1}{\mathrm{Iv}} 3\ \mathrm{V}x\frac{\mathrm{dIt}}{\mathrm{dt}},$$

where Hct is the hematocrit (45%) and Iv is the initial fluorescence intensity of the ROI within the vessel, It is the intensity of the ROI within the brain at time t, and V is the vessel volume, assuming 1 g of brain is equivalent to 50 cm^2.

Brain uptake of Alexa Fluor 555–cadaverine

For intravenous Alexa Fluor 555–cadaverine tracer injection and detection, mice were anesthetized with ketamine and xylazine at 180 mg/kg and 10 mg/kg of body weight, respectively, and 50 µl Alexa Fluor 555–cadaverine (1 mg/ml) was injected into the retro-orbital venous sinus in mice as described previously (Bell et al., 2012; Montagne et al., 2018). For P8 mice, 40 µl Alexa Fluor 555–cadaverine (1 mg/ml) was injected i.p. Cadaverine was allowed to circulate for 20 min in adult mice and 2 h in postnatal mice, respectively. Mice were then perfused intracardially with 4% PFA in PBS. Eyes from P8 animals were fixed in 4% PFA for 2 h at room temperature before retina isolation in PBS. Brains were postfixed at room temperature in 4% PFA for 3 h. For cadaverine detection, whole brains and isolated retinas (mounted in PBS) were imaged using a dissecting microscope with an attached fluorescent lamp and a Texas Red filter and subsequently processed for immunostaining. Cadaverine leakage was quantified by measuring mean fluorescence intensity in reconstructed 10-µm maximum projection z-stacks from four to six randomly selected fields in the cortex from four nonadjacent sections (~100 µm apart).

MRI

All MRI scans were performed using our MR Solutions 7T PET MR system (bore size ~24 mm, up to 600 $\mathrm{mT.m^{-1}}$ maximum gradient) and a 20-mm internal diameter quadrature birdcage mouse head coil. Mice were anesthetized by 1–1.2% isoflurane in air. Respiration rate (80.0 ± 10.0 breaths per min) and body temperature (36.5 ± 0.5°C) were monitored during the experiments, as we described previously (Montagne et al., 2018). The sequences were collected in the following order: T2-weighted imaging (2D fast spin echo; time repetition [TR]/time echo [TE], 4,000/26 ms; 32 slices; slice thickness, 300 µm; in-plane resolution, 100 × 70 μm^2) to obtain structural images followed by a dynamic contrast-enhanced (DCE) protocol for the brain vessel permeability assessment. Total imaging time was ~30 min per mouse.

As previously described (Montagne et al., 2018), the DCE-MRI imaging protocol was performed coronally within the dorsal hippocampus region and included measurement of precontrast T1 values using a variable flip angle fast low-angle shot (FLASH) sequence (flip angle, 5°, 10°, 15°, 30°, and 45°; TE 3 ms, slice thickness 1 mm, in-plane resolution 60 × 120 μm^2), followed by a dynamic series of 180 T1-weighted images with identical geometry and a temporal resolution of 5.1 s (FLASH, TR/TE, 20/3 ms; flip angle, 15°; slice thickness, 1 mm; in-plane resolution, 60 × 120 μm^2). A bolus dose (140 µl) of 0.5 mmol/kg gadolinium diethylenetriamine pentaacetic acid (Gd-DTPA diluted in saline 1:6) was injected into the tail vein at a rate of 600 µl/min using a power injector. DCE images were collected within 15 min of the injection.

MRI postprocessing analysis of BBB permeability to gadolinium

T1 mapping

T1 relaxation times were estimated using the variable flip angle method, before Gd-DTPA injection, with a series of FLASH images with varying flip angle and constant TR and TE, as previously described (Montagne et al., 2018, 2015; Nation et al., 2019; Montagne et al., 2020).

K_{trans} *mapping*

We determined the capillary permeability transfer constant, K_{trans}, to intravenously injected gadolinium-based contrast agent in both the dorsal hippocampus and primary somatosensory cortex using a modified method as we reported in humans with the postprocessing Patlak analysis (Montagne et al., 2015; Nation et al., 2019; Montagne et al., 2020). We determined the arterial input functions (AIFs) in each mouse from the common carotid artery, as previously reported (Nikolakopoulou et al., 2019; Montagne et al., 2018). Individual AIF curves are particularly important for calculating accurately the K_{trans} values if blood flow and volume are influenced by age or a pathological process.

The present Patlak analysis requires that the tracer's diffusion (Gd-DTPA) across the capillary vessel wall remains unidirectional during the acquisition time. The total tracer concentration in the brain tissue, $C_{tissue}(t)$, can be described as a function of the vascular concentration $C_{AIF}(t)$, the intravascular blood volume v_p, and a transfer constant K_{trans} that represents the flow from the intravascular to the extravascular space using the following equation:

$$Ctissue(t) = Ktrans\int_0^t CAIF(\tau)d\tau + \nu p \cdot CAIF(t).$$

Postprocessing of the collected DCE-MRI data was performed using in-house DCE processing software (Rocketship) implemented in MATLAB version R2019b (Barnes et al., 2015).

Behavioral tests

Burrowing

This was performed as we described previously (Sagare et al., 2013). To assess burrowing behavior, mice were individually placed in cages equipped with a burrow made from a 200-mm-long and 70-mm-diameter tube of polyvinyl chloride plastic with one end enclosed. The burrow was filled with 200 g of mouse food pellets, and the mice were allowed to burrow for 2 h right before the beginning of the dark cycle. The weight of the remaining food pellets inside the burrow was determined to obtain a measurement of the food amount burrowed.

Nest construction

This was performed as we previously reported (Sagare et al., 2013; Winkler et al., 2015). 2 h after the beginning of the dark cycle, the animals were individually placed in clean home cages with a single nestlet. Nests were assessed the next morning and evaluated following the five-point scale as we described in detail (Winkler et al., 2015).

Novel object location

This was performed as we have previously reported (Sagare et al., 2013; Bell et al., 2010; Nikolakopoulou et al., 2019). Animals were placed in a 30-cm^3 box and allowed to habituate to the testing area for 10 min. Animals were then placed back in their cages, and two identical ~5 × 5-cm objects were placed in the top left and right corner of the testing area. Animals were allowed to explore the two objects in the testing area for 5 min before being returned to their cages. After a 1-h interval, one of the objects was relocated, and the animals were allowed to explore the testing area once again for 3 min. After each trial, the testing area and the objects were thoroughly cleaned with a 70% ethanol solution. All trials, including habituation, were recorded with a high-resolution camera, and the amount of time each animal spent exploring the objects was analyzed. Any animal that presented a preference for either of the two identical objects, before replacement with the novel location, was eliminated from the analysis.

Novel object recognition

This was performed as we have previously reported, with modifications (Sagare et al., 2013; Bell et al., 2010; Montagne et al., 2018). Briefly, animals were placed in a 30-cm^3 box and allowed to habituate to the testing area for 10 min. Animals were then placed back in their cages, and two identical ~5 × 5-cm objects were placed in the top left and right corner of the testing area. Animals were allowed to explore the two objects in the testing area for 5 min before being returned to their cages. After a 1-h interval, one of the objects was replaced with a new object (different shape and color), and the animals were allowed to explore the testing area once again for 3 min. After each trial, the testing area and the objects were thoroughly cleaned with a 70% ethanol solution. All the trials, including habituation, were recorded with a high-resolution camera, and the amount of time each animal spent exploring the objects was analyzed. Any animal that presented a preference for either of the two identical objects, before replacement with the novel object/location, was eliminated from the analysis.

Statistical analysis

Sample sizes were calculated using nQUERY assuming a two-sided α-level of 0.05, 80% power, and homogeneous variances for the two samples to be compared, with the means and common SD for different parameters predicted from published data and our previous studies (Montagne et al., 2018; Nikolakopoulou et al., 2019; Kisler et al., 2017). Data are presented as mean ± SEM as indicated in the figure legends. For parametric comparison between two groups, an F test was conducted to determine the similarity in the variances between the groups that are statistically compared, and statistical significance was analyzed by Student's *t* test. For multiple comparisons, Bartlett's test for equal variances was used to determine the variances between the multiple groups, and one-way ANOVA followed by Bonferroni's post hoc test was used to test statistical significance using GraphPad Prism 8.3.1 software. Data were tested for normality using the Shapiro–Wilk test. A P value of less than 0.05 was considered statistically significant. For behavioral analysis, the power is 99.5% in Fig. 1 and between 95% and 99.5% in Figs. 2 and 4.

Data and materials availability

All data are available in the main text or supplemental material.

Online supplemental material

Fig. S1 shows an intact BBB and microvascular pattern in *Lrp1*$^{lox/lox}$*; Tie2-Cre* mice at P8, intact microvascular density in 2-mo-old *Lrp1*$^{lox/lox}$*; Tie2-Cre* mice, and BBB breakdown in 1-mo-old *Lrp1*$^{lox/lox}$*; Tie2-Cre* mice. Fig. S2 shows pericyte and astrocyte endfeet capillary and MFSD2a and GLUT1 levels in brain capillaries in *Lrp1*$^{lox/lox}$*; Tie2-Cre* and littermate controls. Fig. S3 shows neuronal degeneration in 3-mo-old *Lrp1*$^{lox/lox}$*; Tie2-Cre* mice after endothelial-specific Lrp1 deletion. Fig. S4 shows loss of collagen IV and hemosiderin deposits in *Lrp1*$^{lox/lox}$*; Tie2-Cre* mice and additional characterization of reagents used in Fig. 4. Fig. S5 shows reversal of BBB breakdown in *Lrp1*$^{lox/lox}$*; Tie2-Cre* mice after short-term treatment with the CypA inhibitor cyclosporine A. Table S1 shows primary and secondary antibodies used for immunohistochemistry.

Acknowledgments

The work of B.V. Zlokovic is supported by the National Institutes of Health (grants R01NS034467, R01AG039452, R01AG023084, R01NS100459, and P01AG052350) and the Fondation Leducq Transatlantic Network of Excellence for the Study of Perivascular Spaces in Small Vessel Disease (reference number 16 CVD 05).

Author contributions: A.M. Nikolakopoulou, Y. Wang, Q. Ma, and Z. Zhao designed and performed experiments and analyzed data. A.P. Sagare, A. Montagne, M.T. Huuskonen, S.V. Rege, and Z. Dai performed experiments and analyzed data. K. Kisler analyzed data. J. Körbelin provided AAV-GFP and AAV-m*LRP1* viruses. J. Herz provided the *LRP1*$^{lox/lox}$ mice. A.M. Nikolakopoulou and Z. Zhao contributed to writing sections of the manuscript. Z. Zhao and B.V. Zlokovic designed all experiments and analyzed data, and B.V. Zlokovic wrote the paper.

Disclosures: J. Körbelin reported personal fees from Boehringer Ingelheim Pharma outside the submitted work; in addition, J. Körbelin had a patent number 10696717 issued and a patent to 10688151 issued. J. Herz reported a patent to 7192714 issued and a patent to 7056688 issued. No other disclosures were reported.

Submitted: 15 October 2020
Revised: 21 November 2020
Accepted: 24 November 2020

References

Aleksinskaya, M.A., E.E.H. van Faassen, J. Nelissen, B.J.A. Janssen, J.G.R. De Mey, R. Hanemaaijer, T. Rabelink, and A.J. van Zonneveld. 2013. Identification of free nitric oxide radicals in rat bone marrow: implications for progenitor cell mobilization in hypertension. *PLoS One.* 8: e57761. https://doi.org/10.1371/journal.pone.0057761

Barnes, S.R., T.S.C. Ng, N. Santa-Maria, A. Montagne, B.V. Zlokovic, and R.E. Jacobs. 2015. ROCKETSHIP: a flexible and modular software tool for the planning, processing and analysis of dynamic MRI studies. *BMC Med. Imaging.* 15:19. https://doi.org/10.1186/s12880-015-0062-3

Bell, R.D., E.A. Winkler, A.P. Sagare, I. Singh, B. LaRue, R. Deane, and B.V. Zlokovic. 2010. Pericytes control key neurovascular functions and neuronal phenotype in the adult brain and during brain aging. *Neuron.* 68:409–427. https://doi.org/10.1016/j.neuron.2010.09.043

Bell, R.D., E.A. Winkler, I. Singh, A.P. Sagare, R. Deane, Z. Wu, D.M. Holtzman, C. Betsholtz, A. Armulik, J. Sallstrom, et al. 2012. Apolipoprotein E controls cerebrovascular integrity via cyclophilin A. *Nature.* 485: 512–516. https://doi.org/10.1038/nature11087

Ben-Zvi, A., B. Lacoste, E. Kur, B.J. Andreone, Y. Mayshar, H. Yan, and C. Gu. 2014. Mfsd2a is critical for the formation and function of the blood-brain barrier. *Nature.* 509:507–511. https://doi.org/10.1038/nature13324

Boucher, P., M. Gotthardt, W.-P. Li, R.G.W. Anderson, and J. Herz. 2003. LRP: role in vascular wall integrity and protection from atherosclerosis. *Science.* 300:329–332. https://doi.org/10.1126/science.1082095

Cortes-Canteli, M., J. Paul, E.H. Norris, R. Bronstein, H.J. Ahn, D. Zamolodchikov, S. Bhuvanendran, K.M. Fenz, and S. Strickland. 2010. Fibrinogen and beta-amyloid association alters thrombosis and fibrinolysis: a possible contributing factor to Alzheimer's disease. *Neuron.* 66:695–709. https://doi.org/10.1016/j.neuron.2010.05.014

Deane, R., S. Du Yan, R.K. Submamaryan, B. LaRue, S. Jovanovic, E. Hogg, D. Welch, L. Manness, C. Lin, J. Yu, et al. 2003. RAGE mediates amyloid-beta peptide transport across the blood-brain barrier and accumulation in brain. *Nat. Med.* 9:907–913. https://doi.org/10.1038/nm890

Deane, R., Z. Wu, A. Sagare, J. Davis, S. Du Yan, K. Hamm, F. Xu, M. Parisi, B. LaRue, H.W. Hu, et al. 2004. LRP/amyloid beta-peptide interaction mediates differential brain efflux of Abeta isoforms. *Neuron.* 43: 333–344. https://doi.org/10.1016/j.neuron.2004.07.017

Demeule, M., J.-C. Currie, Y. Bertrand, C. Ché, T. Nguyen, A. Régina, R. Gabathuler, J.-P. Castaigne, and R. Béliveau. 2008. Involvement of the low-density lipoprotein receptor-related protein in the transcytosis of the brain delivery vector angiopep-2. *J. Neurochem.* 106:1534–1544. https://doi.org/10.1111/j.1471-4159.2008.05492.x

Donahue, J.E., S.L. Flaherty, C.E. Johanson, J.A. Duncan III, G.D. Silverberg, M.C. Miller, R. Tavares, W. Yang, Q. Wu, E. Sabo, et al. 2006. RAGE, LRP-1, and amyloid-beta protein in Alzheimer's disease. *Acta Neuropathol.* 112:405–415. https://doi.org/10.1007/s00401-006-0115-3

Famiglio, L., L. Racusen, B. Fivush, K. Solez, and R. Fisher. 1989. Central nervous system toxicity of cyclosporine in a rat model. *Transplantation.* 48:316–320. https://doi.org/10.1097/00007890-198908000-00025

Fullerton, S.M., G.A. Shirman, W.J. Strittmatter, and W.D. Matthew. 2001. Impairment of the blood-nerve and blood-brain barriers in apolipoprotein e knockout mice. *Exp. Neurol.* 169:13–22. https://doi.org/10.1006/exnr.2001.7631

Gali, C.C., E. Fanaee-Danesh, M. Zandl-Lang, N.M. Albrecher, C. Tam-Amersdorfer, A. Stracke, V. Sachdev, F. Reichmann, Y. Sun, A. Avdili, et al. 2019. Amyloid-beta impairs insulin signaling by accelerating autophagy-lysosomal degradation of LRP-1 and IR-β in blood-brain barrier endothelial cells in vitro and in 3XTg-AD mice. *Mol. Cell. Neurosci.* 99:103390. https://doi.org/10.1016/j.mcn.2019.103390

Gonias, S.L., and W.M. Campana. 2014. LDL receptor-related protein-1: a regulator of inflammation in atherosclerosis, cancer, and injury to the nervous system. *Am. J. Pathol.* 184:18–27. https://doi.org/10.1016/j.ajpath.2013.08.029

Halliday, M.R., S.V. Rege, Q. Ma, Z. Zhao, C.A. Miller, E.A. Winkler, and B.V. Zlokovic. 2016. Accelerated pericyte degeneration and blood-brain barrier breakdown in apolipoprotein E4 carriers with Alzheimer's disease. *J. Cereb. Blood Flow Metab.* 36:216–227. https://doi.org/10.1038/jcbfm.2015.44

Herz, J., and D.K. Strickland. 2001. LRP: a multifunctional scavenger and signaling receptor. *J. Clin. Invest.* 108:779–784. https://doi.org/10.1172/JCI200113992

Herz, J., U. Hamann, S. Rogne, O. Myklebost, H. Gausepohl, and K.K. Stanley. 1988. Surface location and high affinity for calcium of a 500-kd liver membrane protein closely related to the LDL-receptor suggest a physiological role as lipoprotein receptor. *EMBO J.* 7:4119–4127. https://doi.org/10.1002/j.1460-2075.1988.tb03306.x

Jaeger, L.B., S. Dohgu, M.C. Hwang, S.A. Farr, M.P. Murphy, M.A. Fleegal-DeMotta, J.L. Lynch, S.M. Robinson, M.L. Niehoff, S.N. Johnson, et al. 2009. Testing the neurovascular hypothesis of Alzheimer's disease: LRP-1 antisense reduces blood-brain barrier clearance, increases brain levels of amyloid-beta protein, and impairs cognition. *J. Alzheimers Dis.* 17:553–570. https://doi.org/10.3233/JAD-2009-1074

Jambusaria, A., Z. Hong, L. Zhang, S. Srivastava, A. Jana, P.T. Toth, Y. Dai, A.B. Malik, and J. Rehman. 2020. Endothelial heterogeneity across distinct vascular beds during homeostasis and inflammation. *eLife.* 9:e51413. https://doi.org/10.7554/eLife.51413

Kalucka, J., L.P.M.H. de Rooij, J. Goveia, K. Rohlenova, S.J. Dumas, E. Meta, N.V. Conchinha, F. Taverna, L.-A. Teuwen, K. Veys, et al. 2020. Single-Cell Transcriptome Atlas of Murine Endothelial Cells. *Cell.* 180:764–779.e20. https://doi.org/10.1016/j.cell.2020.01.015

Kisanuki, Y.Y., R.E. Hammer, J. Miyazaki, S.C. Williams, J.A. Richardson, and M. Yanagisawa. 2001. Tie2-Cre transgenic mice: a new model for endothelial cell-lineage analysis in vivo. *Dev. Biol.* 230:230–242. https://doi.org/10.1006/dbio.2000.0106

Kisler, K., A.R. Nelson, S.V. Rege, A. Ramanathan, Y. Wang, A. Ahuja, D. Lazic, P.S. Tsai, Z. Zhao, Y. Zhou, et al. 2017. Pericyte degeneration leads to neurovascular uncoupling and limits oxygen supply to brain. *Nat. Neurosci.* 20:406–416. https://doi.org/10.1038/nn.4489

Körbelin, J., G. Dogbevia, S. Michelfelder, D.A. Ridder, A. Hunger, J. Wenzel, H. Seismann, M. Lampe, J. Bannach, M. Pasparakis, et al. 2016. A brain microvasculature endothelial cell-specific viral vector with the potential to treat neurovascular and neurological diseases. *EMBO Mol. Med.* 8:609–625. https://doi.org/10.15252/emmm.201506078

Li, G.-W., D. Burkhardt, C. Gross, and J.S. Weissman. 2014. Quantifying absolute protein synthesis rates reveals principles underlying allocation of cellular resources. *Cell.* 157:624–635. https://doi.org/10.1016/j.cell.2014.02.033

Lillis, A.P., L.B. Van Duyn, J.E. Murphy-Ullrich, and D.K. Strickland. 2008. LDL receptor-related protein 1: unique tissue-specific functions revealed by selective gene knockout studies. *Physiol. Rev.* 88:887–918. https://doi.org/10.1152/physrev.00033.2007

Lim, S.W., K.C. Doh, L. Jin, S.G. Piao, S.B. Heo, Y.F. Zheng, S.K. Bae, B.H. Chung, and C.W. Yang. 2013. Oral administration of ginseng ameliorates cyclosporine-induced pancreatic injury in an experimental mouse model. *PLoS One.* 8:e72685. https://doi.org/10.1371/journal.pone.0072685

Ma, S., H.J. Kwon, H. Johng, K. Zang, and Z. Huang. 2013. Radial glial neural progenitors regulate nascent brain vascular network stabilization via inhibition of Wnt signaling. *PLoS Biol.* 11:e1001469. https://doi.org/10.1371/journal.pbio.1001469

Mantuano, E., M.S. Lam, and S.L. Gonias. 2013. LRP1 assembles unique co-receptor systems to initiate cell signaling in response to tissue-type plasminogen activator and myelin-associated glycoprotein. *J. Biol. Chem.* 288:34009–34018. https://doi.org/10.1074/jbc.M113.509133

Mao, H., P. Lockyer, W.H.D. Townley-Tilson, L. Xie, and X. Pi. 2016. LRP1 Regulates Retinal Angiogenesis by Inhibiting PARP-1 Activity and Endothelial Cell Proliferation. *Arterioscler. Thromb. Vasc. Biol.* 36:350–360. https://doi.org/10.1161/ATVBAHA.115.306713

Mao, H., P. Lockyer, L. Li, C.M. Ballantyne, C. Patterson, L. Xie, and X. Pi. 2017. Endothelial LRP1 regulates metabolic responses by acting as a co-activator of PPARγ. *Nat. Commun.* 8:14960. https://doi.org/10.1038/ncomms14960

Meng, H., X. Zhang, S.J. Lee, D.K. Strickland, D.A. Lawrence, and M.M. Wang. 2010. Low density lipoprotein receptor-related protein-1 (LRP1) regulates thrombospondin-2 (TSP2) enhancement of Notch3 signaling. *J. Biol. Chem.* 285:23047–23055. https://doi.org/10.1074/jbc.M110.144634

Millay, D.P., M.A. Sargent, H. Osinska, C.P. Baines, E.R. Barton, G. Vuagniaux, H.L. Sweeney, J. Robbins, and J.D. Molkentin. 2008. Genetic and pharmacologic inhibition of mitochondrial-dependent necrosis attenuates muscular dystrophy. *Nat. Med.* 14:442–447. https://doi.org/10.1038/nm1736

Montagne, A., S.R. Barnes, M.D. Sweeney, M.R. Halliday, A.P. Sagare, Z. Zhao, A.W. Toga, R.E. Jacobs, C.Y. Liu, L. Amezcua, et al. 2015. Blood-brain barrier breakdown in the aging human hippocampus. *Neuron.* 85:296–302. https://doi.org/10.1016/j.neuron.2014.12.032

Montagne, A., A.M. Nikolakopoulou, Z. Zhao, A.P. Sagare, G. Si, D. Lazic, S.R. Barnes, M. Daianu, A. Ramanathan, A. Go, et al. 2018. Pericyte degeneration causes white matter dysfunction in the mouse central nervous system. *Nat. Med.* 24:326–337. https://doi.org/10.1038/nm.4482

Montagne, A., D.A. Nation, A.P. Sagare, G. Barisano, M.D. Sweeney, A. Chakhoyan, M. Pachicano, E. Joe, A.R. Nelson, L.M. D'Orazio, et al. 2020. APOE4 leads to blood-brain barrier dysfunction predicting cognitive decline. *Nature.* 581:71–76. https://doi.org/10.1038/s41586-020-2247-3

Nation, D.A., M.D. Sweeney, A. Montagne, A.P. Sagare, L.M. D'Orazio, M. Pachicano, F. Sepehrband, A.R. Nelson, D.P. Buennagel, M.G. Harrington, et al. 2019. Blood-brain barrier breakdown is an early biomarker of human cognitive dysfunction. *Nat. Med.* 25:270–276. https://doi.org/10.1038/s41591-018-0297-y

Nikolakopoulou, A.M., Z. Zhao, A. Montagne, and B.V. Zlokovic. 2017. Regional early and progressive loss of brain pericytes but not vascular smooth muscle cells in adult mice with disrupted platelet-derived growth factor receptor-β signaling. *PLoS One.* 12:e0176225. https://doi.org/10.1371/journal.pone.0176225

Nikolakopoulou, A.M., A. Montagne, K. Kisler, Z. Dai, Y. Wang, M.T. Huuskonen, A.P. Sagare, D. Lazic, M.D. Sweeney, P. Kong, et al. 2019. Pericyte loss leads to circulatory failure and pleiotrophin depletion causing neuron loss. *Nat. Neurosci.* 22:1089–1098. https://doi.org/10.1038/s41593-019-0434-z

Nitta, T., M. Hata, S. Gotoh, Y. Seo, H. Sasaki, N. Hashimoto, M. Furuse, and S. Tsukita. 2003. Size-selective loosening of the blood-brain barrier in claudin-5-deficient mice. *J. Cell Biol.* 161:653–660. https://doi.org/10.1083/jcb.200302070

Pflanzner, T., M.C. Janko, B. André-Dohmen, S. Reuss, S. Weggen, A.J.M. Roebroek, C.R.W. Kuhlmann, and C.U. Pietrzik. 2011. LRP1 mediates bidirectional transcytosis of amyloid-β across the blood-brain barrier. *Neurobiol. Aging.* 32:2323.e1–2323.e11. https://doi.org/10.1016/j.neurobiolaging.2010.05.025

Ruck, T., S. Bittner, L. Epping, A.M. Herrmann, and S.G. Meuth. 2014. Isolation of primary murine brain microvascular endothelial cells. *J. Vis. Exp.* (93):e52204. https://doi.org/10.3791/52204

Sabbagh, M.F., J.S. Heng, C. Luo, R.G. Castanon, J.R. Nery, A. Rattner, L.A. Goff, J.R. Ecker, and J. Nathans. 2018. Transcriptional and epigenomic landscapes of CNS and non-CNS vascular endothelial cells. *eLife.* 7:e36187. https://doi.org/10.7554/eLife.36187

Sagare, A.P., R.D. Bell, Z. Zhao, Q. Ma, E.A. Winkler, A. Ramanathan, and B.V. Zlokovic. 2013. Pericyte loss influences Alzheimer-like neurodegeneration in mice. *Nat. Commun.* 4:2932. https://doi.org/10.1038/ncomms3932

Santos, J.B., and P.E. Schauwecker. 2003. Protection provided by cyclosporin A against excitotoxic neuronal death is genotype dependent. *Epilepsia.* 44:995–1002. https://doi.org/10.1046/j.1528-1157.2003.66302.x

Schindelin, J., I. Arganda-Carreras, E. Frise, V. Kaynig, M. Longair, T. Pietzsch, S. Preibisch, C. Rueden, S. Saalfeld, B. Schmid, et al. 2012. Fiji: an open-source platform for biological-image analysis. *Nat. Methods.* 9: 676–682. https://doi.org/10.1038/nmeth.2019

Senatorov, V.V. Jr., A.R. Friedman, D.Z. Milikovsky, J. Ofer, R. Saar-Ashkenazy, A. Charbash, N. Jahan, G. Chin, E. Mihaly, J.M. Lin, et al. 2019. Blood-brain barrier dysfunction in aging induces hyperactivation of TGFβ signaling and chronic yet reversible neural dysfunction. *Sci. Transl. Med.* 11:eaaw8283. https://doi.org/10.1126/scitranslmed.aaw8283

Shibata, M., S. Yamada, S.R. Kumar, M. Calero, J. Bading, B. Frangione, D.M. Holtzman, C.A. Miller, D.K. Strickland, J. Ghiso, and B.V. Zlokovic. 2000. Clearance of Alzheimer's amyloid-ss(1-40) peptide from brain by LDL receptor-related protein-1 at the blood-brain barrier. *J. Clin. Invest.* 106:1489–1499. https://doi.org/10.1172/JCI10498

Shin, Y., S.H. Choi, E. Kim, E. Bylykbashi, J.A. Kim, S. Chung, D.Y. Kim, R.D. Kamm, and R.E. Tanzi. 2019. Blood-Brain Barrier Dysfunction in a 3D In Vitro Model of Alzheimer's Disease. *Adv. Sci. (Weinh.).* 6:1900962. https://doi.org/10.1002/advs.201900962

Stanciu, C., A. Trifan, C. Muzica, and C. Sfarti. 2019. Efficacy and safety of alisporivir for the treatment of hepatitis C infection. *Expert Opin. Pharmacother.* 20:379–384. https://doi.org/10.1080/14656566.2018.1560424

Storck, S.E., S. Meister, J. Nahrath, J.N. Meißner, N. Schubert, A. Di Spiezio, S. Baches, R.E. Vandenbroucke, Y. Bouter, I. Prikulis, et al. 2016. Endothelial LRP1 transports amyloid-β(1-42) across the blood-brain barrier. *J. Clin. Invest.* 126:123–136. https://doi.org/10.1172/JCI81108

Strickland, D.K., and S.C. Muratoglu. 2016. LRP in Endothelial Cells: A Little Goes a Long Way. *Arterioscler. Thromb. Vasc. Biol.* 36:213–216. https://doi.org/10.1161/ATVBAHA.115.306895

Sweeney, M.D., K. Kisler, A. Montagne, A.W. Toga, and B.V. Zlokovic. 2018. The role of brain vasculature in neurodegenerative disorders. *Nat. Neurosci.* 21:1318–1331. https://doi.org/10.1038/s41593-018-0234-x

Tiepolo, T., A. Angelin, E. Palma, P. Sabatelli, L. Merlini, L. Nicolosi, F. Finetti, P. Braghetta, G. Vuagniaux, J.-M. Dumont, et al. 2009. The cyclophilin inhibitor Debio 025 normalizes mitochondrial function, muscle apoptosis and ultrastructural defects in Col6a1-/- myopathic mice. *Br. J. Pharmacol.* 157:1045–1052. https://doi.org/10.1111/j.1476-5381.2009.00316.x

Trost, A., F. Schroedl, S. Lange, F.J. Rivera, H. Tempfer, S. Korntner, C.C. Stolt, M. Wegner, B. Bogner, A. Kaser-Eichberger, et al. 2013. Neural crest origin of retinal and choroidal pericytes. *Invest. Ophthalmol. Vis. Sci.* 54:7910–7921. https://doi.org/10.1167/iovs.13-12946

Ueno, M., T. Nakagawa, B. Wu, M. Onodera, C.-L. Huang, T. Kusaka, N. Araki, and H. Sakamoto. 2010. Transporters in the brain endothelial barrier. *Curr. Med. Chem.* 17:1125–1138. https://doi.org/10.2174/092986710790827816

Van Gool, B., S.E. Storck, S.M. Reekmans, B. Lechat, P.L.S.M. Gordts, L. Pradier, C.U. Pietrzik, and A.J.M. Roebroek. 2019. LRP1 Has a Predominant Role in Production over Clearance of Aβ in a Mouse Model of Alzheimer's Disease. *Mol. Neurobiol.* 56:7234–7245. https://doi.org/10.1007/s12035-019-1594-2

Vandooren, J., N. Geurts, E. Martens, P.E. Van den Steen, S.D. Jonghe, P. Herdewijn, and G. Opdenakker. 2011. Gelatin degradation assay reveals MMP-9 inhibitors and function of O-glycosylated domain. *World J. Biol. Chem.* 2:14–24. https://doi.org/10.4331/wjbc.v2.i1.14

Vanlandewijck, M., L. He, M.A. Mäe, J. Andrae, K. Ando, F. Del Gaudio, K. Nahar, T. Lebouvier, B. Laviña, L. Gouveia, et al. 2018. A molecular atlas of cell types and zonation in the brain vasculature. *Nature.* 554:475–480. https://doi.org/10.1038/nature25739

Wang, X., S.-R. Lee, K. Arai, S.-R. Lee, K. Tsuji, G.W. Rebeck, and E.H. Lo. 2003. Lipoprotein receptor-mediated induction of matrix metalloproteinase by tissue plasminogen activator. *Nat. Med.* 9:1313–1317. https://doi.org/10.1038/nm926

Winkler, E.A., Y. Nishida, A.P. Sagare, S.V. Rege, R.D. Bell, D. Perlmutter, J.D. Sengillo, S. Hillman, P. Kong, A.R. Nelson, et al. 2015. GLUT1 reductions exacerbate Alzheimer's disease vasculo-neuronal dysfunction and degeneration. *Nat. Neurosci.* 18:521–530. https://doi.org/10.1038/nn.3966

Wu, L., Q. Zheng, Y.-Y. Guo, K.-N. Zhang, J. Luo, S. Xiao, W.-J. Li, and M. Yang. 2020. Effect of Zhenxin Xingshui Yizhi Fang on $A\beta_{25-35}$ induced expression of related transporters in HBMEC cell model. *J. Ethnopharmacol.* 260:112783. https://doi.org/10.1016/j.jep.2020.112783

Yamada, K., T. Hashimoto, C. Yabuki, Y. Nagae, M. Tachikawa, D.K. Strickland, Q. Liu, G. Bu, J.M. Basak, D.M. Holtzman, et al. 2008. The low density lipoprotein receptor-related protein 1 mediates uptake of amyloid beta peptides in an in vitro model of the blood-brain barrier cells. *J. Biol. Chem.* 283:34554–34562. https://doi.org/10.1074/jbc.M801487200

Zeisel, A., A.B. Muñoz-Manchado, S. Codeluppi, P. Lönnerberg, G. La Manno, A. Juréus, S. Marques, H. Munguba, L. He, C. Betsholtz, et al. 2015. Cell types in the mouse cortex and hippocampus revealed by single-cell RNA-seq. *Science.* 347:1138–1142. https://doi.org/10.1126/science.aaa1934

Zeisel, A., H. Hochgerner, P. Lönnerberg, A. Johnsson, F. Memic, J. van der Zwan, M. Häring, E. Braun, L.E. Borm, G. La Manno, et al. 2018. Molecular Architecture of the Mouse Nervous System. *Cell.* 174: 999–1014.e22. https://doi.org/10.1016/j.cell.2018.06.021

Zhang, Y., S.A. Sloan, L.E. Clarke, C. Caneda, C.A. Plaza, P.D. Blumenthal, H. Vogel, G.K. Steinberg, M.S.B. Edwards, G. Li, et al. 2016. Purification and Characterization of Progenitor and Mature Human Astrocytes Reveals Transcriptional and Functional Differences with Mouse. *Neuron.* 89:37–53. https://doi.org/10.1016/j.neuron.2015.11.013

Zhao, Z., A.R. Nelson, C. Betsholtz, and B.V. Zlokovic. 2015a. Establishment and Dysfunction of the Blood-Brain Barrier. *Cell.* 163:1064–1078. https://doi.org/10.1016/j.cell.2015.10.067

Zhao, Z., A.P. Sagare, Q. Ma, M.R. Halliday, P. Kong, K. Kisler, E.A. Winkler, A. Ramanathan, T. Kanekiyo, G. Bu, et al. 2015b. Central role for PICALM in amyloid-β blood-brain barrier transcytosis and clearance. *Nat. Neurosci.* 18:978–987. https://doi.org/10.1038/nn.4025

Zhu, D., Y. Su, B. Fu, and H. Xu. 2018. Magnesium Reduces Blood-Brain Barrier Permeability and Regulates Amyloid-β Transcytosis. *Mol. Neurobiol.* 55:7118–7131. https://doi.org/10.1007/s12035-018-0896-0

Zilberberg, A., A. Yaniv, and A. Gazit. 2004. The low density lipoprotein receptor-1, LRP1, interacts with the human frizzled-1 (HFz1) and downregulates the canonical Wnt signaling pathway. *J. Biol. Chem.* 279: 17535–17542. https://doi.org/10.1074/jbc.M311292200

Supplemental material

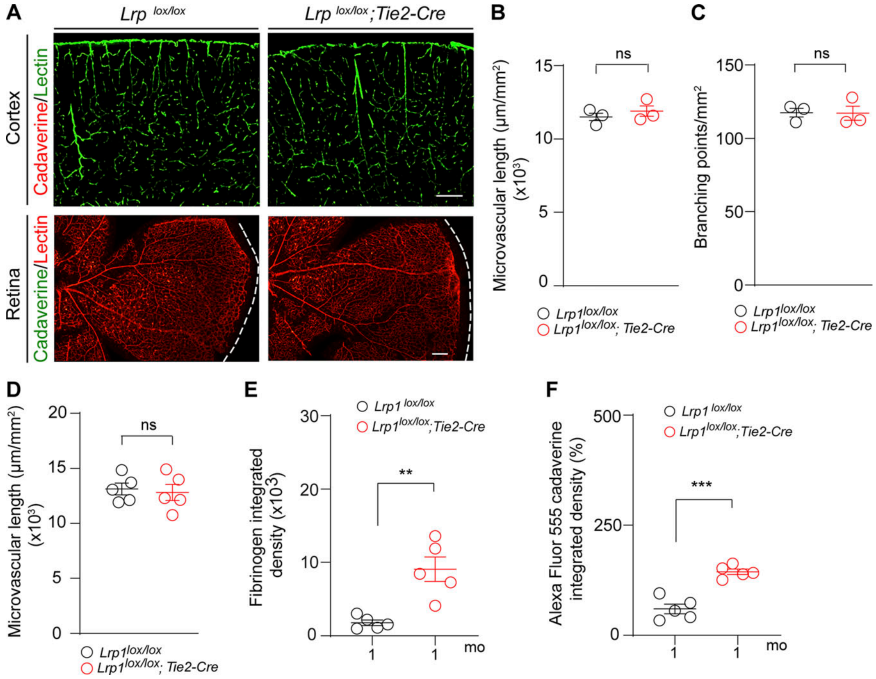

Figure S1. **Intact BBB and microvascular pattern in *Lrp1*$^{lox/lox}$; *Tie2-Cre* mice at P8, intact microvascular density in 2-mo-old *Lrp1*$^{lox/lox}$; *Tie2-Cre* mice, and BBB breakdown in 1-mo-old *Lrp1*$^{lox/lox}$; *Tie2-Cre* mice. (A)** Confocal images of lectin^{+} endothelial microvascular profiles in the cortex (green) and retina (red) in 8-d-old (P8) *Lrp1*$^{lox/lox}$; *Tie2-Cre* and *Lrp1*$^{lox/lox}$ littermate control pups injected intravenously with Alexa Fluor 555–conjugated cadaverine show no BBB leakage of tracer into the cortex (red) or retina (green). Representative images shown are from three mice per group. Scale bars = 200 µm. **(B and C)** Microvascular length (B) and capillary branching points (C) determined in 10-µm-thick cortical tissue sections from P8 *Lrp1*$^{lox/lox}$ and *Lrp1*$^{lox/lox}$; *Tie2-Cre* mice and expressed per square millimeter of tissue. **(D)** Microvascular length in the cortex of 2-mo-old *Lrp1*$^{lox/lox}$ and *Lrp1*$^{lox/lox}$; *Tie2-Cre* mice and expressed per square millimeter of tissue. **(E and F)** Quantification of fibrinogen deposits (E) and leakage of Alexa Fluor 555–conjugated cadaverine tracer (F) deposits in the cortex of 1-mo-old *Lrp1*$^{lox/lox}$; *Tie2-Cre* mice compared with *Lrp1*$^{lox/lox}$ controls. In B–F, data represent mean ± SEM, *n* = 3–5 mice/group; ns, nonsignificant by Student's *t* test; **, $P < 0.01$; ***, $P < 0.001$.

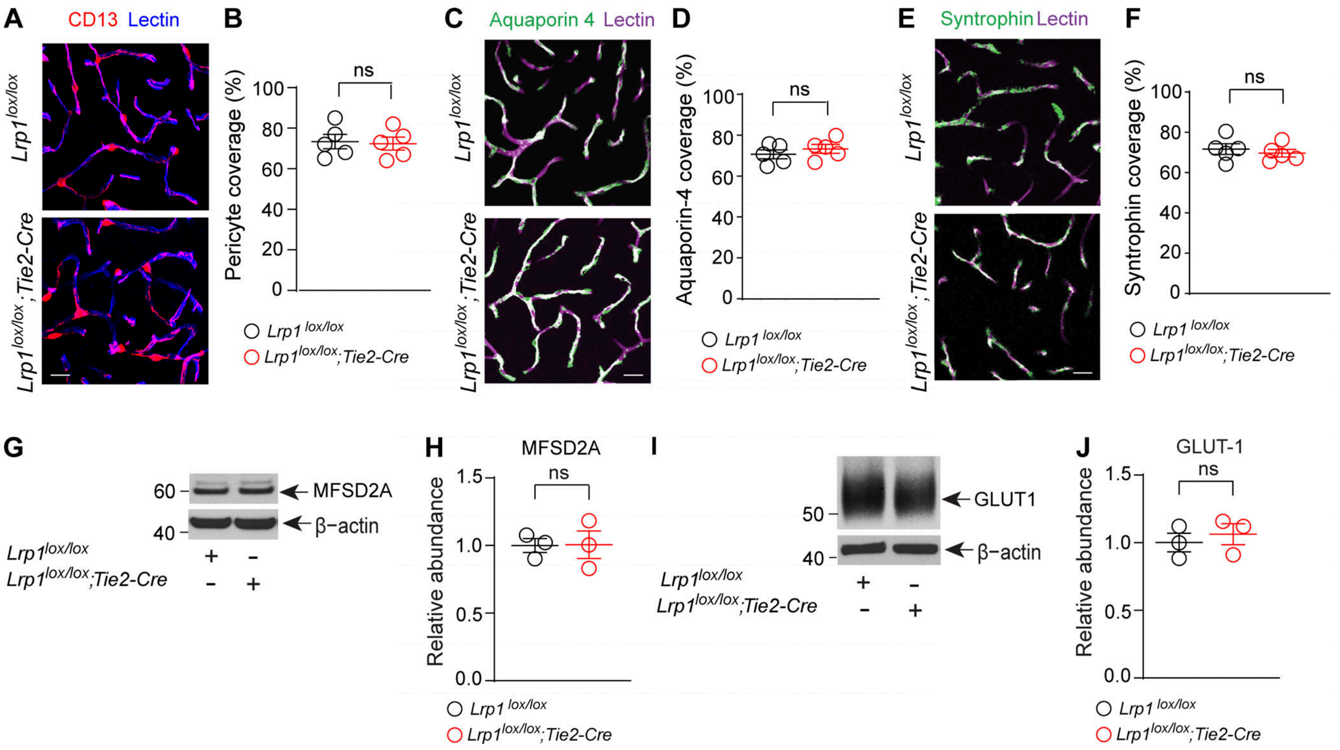

Figure S2. **Additional characterization of *Lrp1*$^{lox/lox}$; *Tie2-Cre* mice. (A and B)** Representative confocal microscopy images of CD13^{+} pericytes (magenta) and lectin^{+} endothelium (blue) in the cortex of 4-mo-old *Lrp1*$^{lox/lox}$; *Tie2-Cre* and *Lrp1*$^{lox/lox}$ littermate control mice (A), and quantification of pericyte coverage of brain capillary (<6 µm in diameter) lectin^{+} endothelial profiles (B). Scale bar = 25 µm. Mean ± SEM, *n* = 5 mice/group. **(C and D)** Representative confocal images of aquaporin 4^{+} astrocyte endfeet (green) and lectin^{+} endothelium (purple) in the cortex of 4-mo-old *Lrp1*$^{lox/lox}$; *Tie2-Cre* and *Lrp1*$^{lox/lox}$ littermate control mice (C) and quantification of astrocytic endfeet aquaporin 4^{+} coverage of brain capillary (<6 µm in diameter) lectin^{+} endothelial profiles (D). Scale bar = 25 µm. Mean ± SEM, *n* = 5 mice/group. **(E and F)** Representative confocal images of α-syntrophin^{+} astrocytic endfeet (green) and lectin^{+} endothelium (purple) in the cortex of 4-mo-old *Lrp1*$^{lox/lox}$; *Tie2-Cre* and *Lrp1*$^{lox/lox}$ littermate control mice (E) and quantification of astrocytic endfeet α-syntrophin^{+} coverage of brain capillary (<6 µm in diameter) lectin^{+} endothelial profiles (F). Scale bar = 25 µm. Mean ± SEM, *n* = 5 mice per group. **(G and H)** Immunoblotting (G) and relative abundance of endothelial major facilitator superfamily domain–containing protein 2 (MSFD2a) using β-actin as a loading control (H) in isolated brain microvessels from 4-mo-old *Lrp1*$^{lox/lox}$; *Tie2-Cre* mice and *Lrp1*$^{lox/lox}$ littermate controls. **(I and J)** Immunoblotting (I) and relative abundance of endothelial glucose transporter 1 (GLUT1) using β-actin as a loading control (J) in isolated brain microvessels from 4-mo-old *Lrp1*$^{lox/lox}$; *Tie2-Cre* mice and *Lrp1*$^{lox/lox}$ littermate controls. In H and J, mean ± SEM, *n* = 3 mice per group. In B, D, F, H, and J, ns, nonsignificant by Student's *t* test.

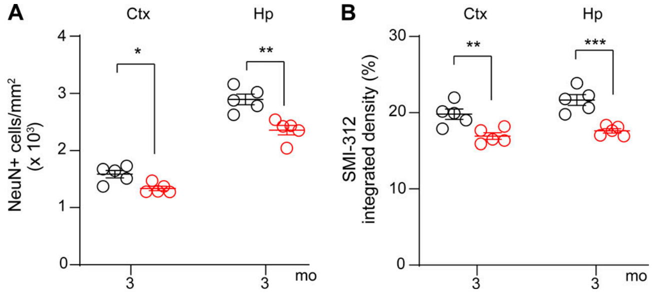

Figure S3. **Neuronal degeneration in 3-mo-old *Lrp1*$^{lox/lox}$; *Tie2-Cre* mice after endothelial-specific *Lrp1* deletion. (A and B)** Quantification of NeuN^{+} neurons (A) and SMI312^{+} neurites (B) in the cortex (Ctx) and hippocampus (Hp) of 3-mo-old *Lrp1*$^{lox/lox}$; *Tie2-Cre* and *Lrp1*$^{lox/lox}$ mice. Mean ± SEM, *n* = 5 mice/group. Significance by Student's *t* test, *, $P < 0.05$; **, $P < 0.01$; ***, $P < 0.001$.

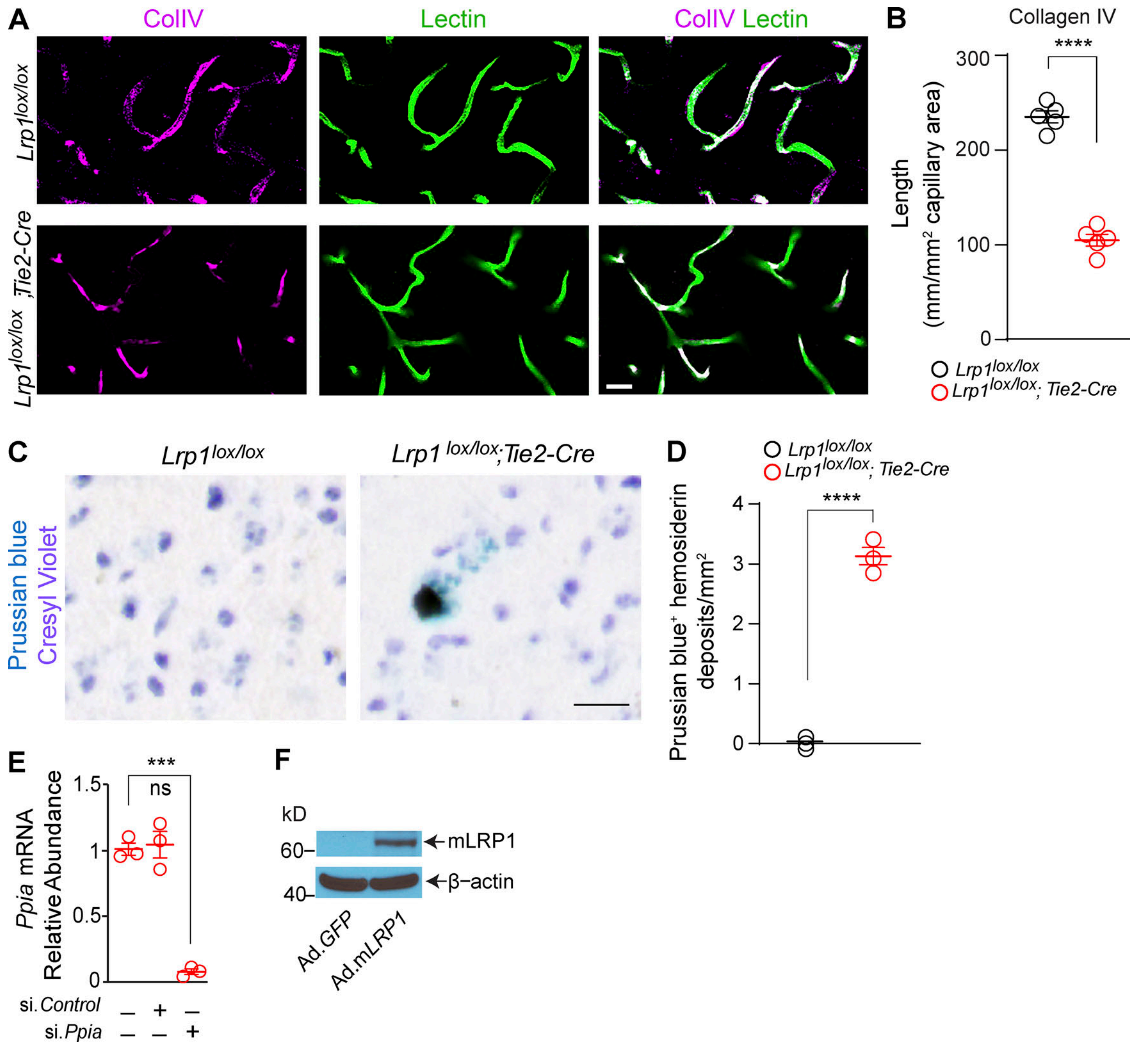

Figure S4. **Loss of collagen IV and hemosiderin deposits in *Lrp1*$^{lox/lox}$*; Tie2-Cre* mice and additional characterization of reagents used in Fig. 4. (A and B)** Immunostaining for collagen IV (CollV; magenta) and fluorescent staining for lectin⁺ endothelium (green) in the cortex of 2-mo-old *Lrp1*$^{lox/lox}$*;Tie2-Cre* and *Lrp1*$^{lox/lox}$ control mice (A), and quantification of collagen IV length on brain capillary (<6 µm in diameter) lectin⁺ endothelial profiles in these mice (B). Scale bar = 25 µm. Mean ± SEM, *n* = 5 mice/group. **(C and D)** Prussian blue hemosiderin deposits in 2-mo-old *Lrp1*$^{lox/lox}$*;Tie2-Cre* mouse and lack of Prussian blue deposits in *Lrp1*$^{lox/lox}$ control (C), and quantification of Prussian blue⁺ hemosiderin deposits in these mice (D). Scale bar = 20 µm. Mean ± SEM, *n* = 3 mice/group. **(E)** Inhibition of *Ppia* mRNA (encoding CypA) by si*Ppia*, but not si*Control,* in brain endothelial cells isolated from 2-mo-old *Lrp1*$^{lox/lox}$*; Tie2-Cre* mice. **(F)** Representative immunoblotting of mLRP1 in brain endothelial cells from 2-mo-old *Lrp1*$^{lox/lox}$*; Tie2-Cre* mice after adenoviral-mediated reexpression with Ad.m*LRP1* but not control Ad.*GFP* virus. Significance by Student's *t* test; ns, not significant; ***, P < 0.001; ****, P < 0.0001.

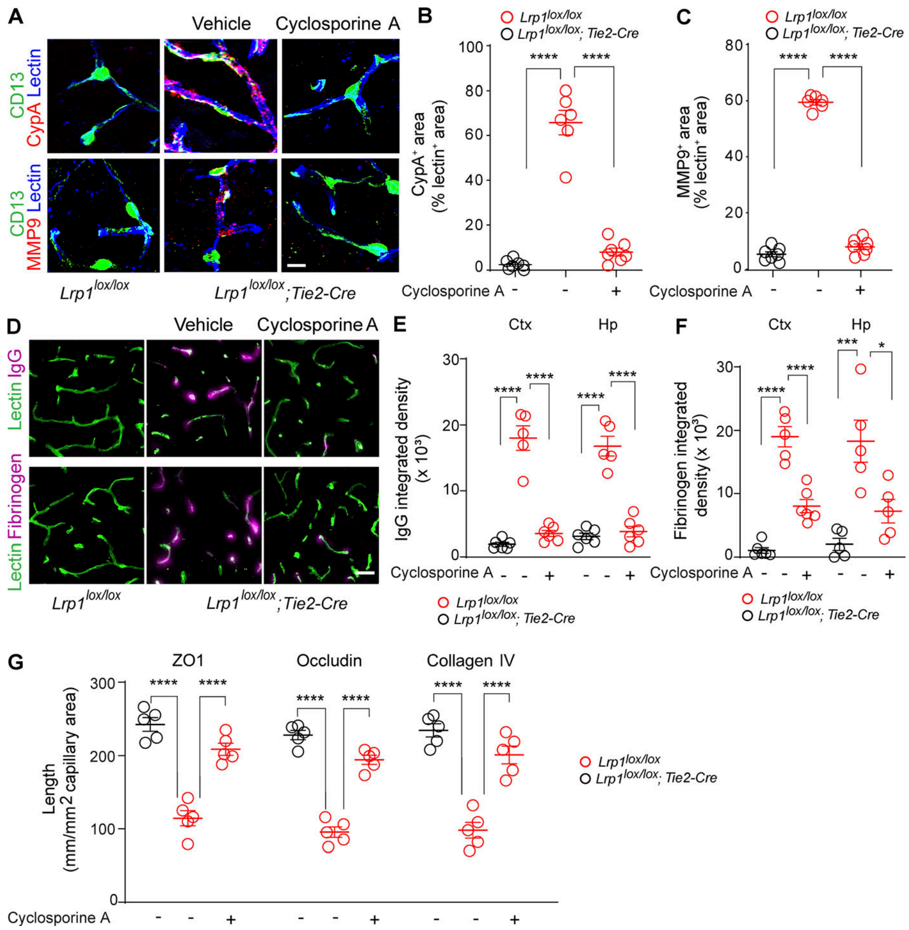

Figure S5. **Short-term treatment with CypA inhibitor cyclosporine A reverses BBB breakdown in *Lrp1*$^{lox/lox}$;*Tie2-Cre* mice. (A–C)** CypA (top, red) and MMP9 (bottom, red) immunostaining in brain capillary (<6 µm in diameter) lectin^{+} endothelium (blue) in the cortex of 2-mo-old *Lrp1*$^{lox/lox}$ control and *Lrp1*$^{lox/lox}$;*Tie2-Cre* mice treated for 7 d with cyclosporine A (see Materials and methods) or vehicle (A), and quantification of CypA (B) and MMP9 (C) fluorescent intensity in brain capillary lectin^{+} endothelium in these mice. Scale bar = 10 µm. Mean ± SEM, *n* = 6–7 mice/group. **(D–F)** IgG (top, purple) and fibrinogen (bottom, purple) immunostaining and lectin^{+} endothelial brain capillary (<6 µm in diameter) profiles (green) in the cortex of 2-mo-old *Lrp1*$^{lox/lox}$ control and *Lrp1*$^{lox/lox}$;*Tie2-Cre* mice treated with cyclosporine A or vehicle (D), and quantification of IgG (E) and fibrinogen (F) perivascular capillary deposits in the cortex (Ctx) and hippocampus (Hp) of these mice. Scale bar = 20 µm. Mean ± SEM, *n* = 5–6 mice/group. **(G)** Quantification of ZO-1, occludin, and collagen IV length on lectin^{+} endothelial capillary profiles in the cortex of 2-mo-old *Lrp1*$^{lox/lox}$;*Tie2-Cre* mice treated with cyclosporine A or vehicle compared with *Lrp1*$^{lox/lox}$. Mean ± SEM, *n* = 5 mice/group. In B, C, and E–G, significance was determined by one-way ANOVA followed by Bonferroni post hoc test, *, $P < 0.05$; ***, $P < 0.001$; ****, $P < 0.0001$.

Table S1 is provided online and lists the primary and secondary antibodies used for immunohistochemistry.